

Hard and soft materials: Putting consistent van der Waals density functionals to work

Carl M. Frostenson*,¹ Erik Jedvik Granhed*,^{2,3} Vivekanand Shukla,¹
Pär A. T. Olsson,^{4,5} Elsebeth Schröder,¹ and Per Hyldgaard¹

¹*Department of Microtechnology and Nanoscience - MC2,
Chalmers University of Technology, SE-41296 Gothenburg, Sweden**

²*Department of Materials Science and Engineering,
KTH Royal Institute of Technology, SE-10044 Stockholm, Sweden*

³*Department of Physics, Chalmers University of Technology, SE-41296 Gothenburg, Sweden**

⁴*Materials Science and Applied Mathematics, Malmö University, SE-205 06 Malmö, Sweden*

⁵*Division of Mechanics, Lund University, Box 118, SE-221 00 Lund, Sweden*

(Dated: January 5, 2022)

We present the idea and illustrate potential benefits of having a tool chain of closely related regular, unscreened and screened hybrid exchange-correlation (XC) functionals, all within the consistent formulation of the van der Waals density functional (vdW-DF) method [JPCM 32, 393001 (2020)]. Use of this chain of nonempirical XC functionals allows us to map when the inclusion of truly nonlocal exchange and of truly nonlocal correlation is important. Here we begin the mapping by addressing hard and soft material challenges: magnetic elements, perovskites, and biomolecular problems. We also predict the structure and polarization for a ferroelectric polymer. To facilitate this work and future broader explorations, we furthermore present a stress formulation for spin vdW-DF and illustrate use of a simple stability-modeling scheme to assert when the prediction of a soft mode (an imaginary-frequency vibrational mode, ubiquitous in perovskites and soft matter) implies a prediction of an actual low-temperature transformation.

I. INTRODUCTION

Modern density functional theory (DFT) calculations seek to describe general matter, ideally with one and the same exchange-correlation (XC) energy functional for all materials, i.e., under a general-purpose hat. Truly nonlocal and strong correlation effects, as well as truly nonlocal (Fock) exchange, play important roles in many systems, where different interaction components compete [1–7]. Some challenges come from the tendency to overly delocalize orbitals in regular, that is, density-explicit functionals, and some from the need to handle strong (local) correlation. These problems can be ameliorated by inclusion of a fraction of Fock exchange in so-called hybrid XC functionals [8–14] or by inclusion of a Hubbard term, in so-called DFT+U [15]. A further long-standing challenge for DFT is a proper and balanced inclusion of van der Waals (vdW) forces [2, 7, 16–22].

It is expected that, at least for now, one must retain both a regular (density-explicit) XC functional, a hybrid XC functional, as well as an option for a Hubbard-U correction in DFT calculations [6]. However, it is also desirable to limit the personal DFT tool box to essentially two to three fixed XC choices of related origin. This is because one can then more easily compare DFT results among different types of materials and more easily gather experience to seek further development [6, 22, 23].

For example, a popular choice is to use XC functionals that originate from the constraint-based formulation of the generalized gradient approximation (GGA) [24–29], by picking PBE [30] as the regular functional, PBE0 [9, 11] as an unscreened hybrid, and HSE [12, 31] as the range-separated hybrid (RSH) that also secures a screening of the long-range Fock-exchange component. This XC tool-chain works when the impact of truly nonlocal-correlation effects can be ignored.

The vdW density functional (vdW-DF) method [4, 13, 16, 22, 23, 32–37] has a systematic inclusion of truly nonlocal correlation effects. Moreover, it now also provides an XC tool chain of closely related consistent vdW-DF [22] XC functionals. That is, the method now has the consistent-exchange vdW-DF-cx [4, 23, 37] (here abbreviated CX) as a current-conserving density-explicit XC starting point, the zero-parameter vdW-DF-cx0p [13, 14] (here abbreviated CX0P) as an associated unscreened nonlocal-correlation hybrid, and the new vdW-DF-ahcx [38] (here abbreviated AHCX) RSH hybrid form. These forms are deliberately kept free of adjustable parameters.

The vdW-DF method and our consistent-vdW-DF tool chain include a balanced density-based account of van der Waals (vdW) forces, starting from the screening insight that reflects the design of semilocal functionals [4, 21–23, 37–39]. It places all of the competing interactions on an equal ground-state DFT foundation, as all terms directly reflect the variation in the ground state electron density $n(\mathbf{r})$. This is true also for CX0P and AHCX, because they use the Kohn-Sham (KS) or-

* Equal contribution

bitals of the underlying density-explicit CX functional in the Fock-exchange evaluation [22, 23]. Moreover, the Fock-exchange mixing in CX0P [14] and (by extension) in AHCX [38] is set from an analysis of the coupling-constant scaling analysis of the correlation-energy term [40], which again is completely specified by the electron density variation [14].

In this paper, we illustrate the general-purpose usefulness of the consistent-vdW-DF XC tool chain (CX/CX0P/AHCX), and we begin work to expand their use for magnetic systems. That is, we provide a formulation of stress in spin vdW-DF calculations and implement it in the planewave-DFT software suite QUANTUM ESPRESSO [41, 42]. We also illustrate an approach to discuss stability in the presence of soft modes, i.e., vibrational modes that have an imaginary frequency when described in a quadratic approximation to the potential energy variation with local deformations. Our approach is inspired by a quantum theory of temperature variations of polarization fluctuations above the ferroelectric transition temperature [43]. We combine Landau-expansion theory [44] with inelastic resonant tunneling [45–50] for a simple, but generic, discussion of materials characterizations in the presence of soft modes.

Accurate determinations of spin and vibrational effects are central requirements for the usefulness of the vdW-DF method. A proper spin-vdW-DF formulation for the XC value E_c^{nl} and for XC-potential components, $v_{c,s=\uparrow,\downarrow}^{\text{nl}}(\mathbf{r})$ is generally needed to accurately describe the atoms, and hence bulk cohesion [51]. However, we also need spin in many materials directly, for example, in magnetic elements and perovskites. For such problems it is desirable to have access to spin-vdW-DF stress results to enable consistent structural optimizations. Similarly, vibrations often directly affect and will at least fine tune material characterizations, as some of us have explicitly demonstrated for transition-metal and perovskite thermophysical properties [51–53].

A broad test, from hard to soft matter, of usefulness of the consistent-vdW-DF tool chain is needed. Structure, polarization, and vibrations are seen as strong discriminators of DFT performance as they directly reflect the electronic structure variation [4, 22, 54–56]. The CX/CX0P/AHCX demonstration and testing goal is pursued by computing material properties using at least two parts of the tool chain (as relevant and possible). We characterize magnetic elements’ structure and cohesion, structure in a ferromagnetic perovskite, as well as the elastic response, vibrations, and phase stability in the nonmagnetic SrTiO₃. The latter has a known phase transition and offers an opportunity for contrasting with the BaZrO₃, which remains cubic all the way down to zero temperature [52, 53]. We furthermore study biomolecular test cases and intercalation in DNA to document that CX is accurate for soft matter, and proceed to predict the structure and polarization response in the ferroelec-

tric polyvinyl-di-fluoride (PVDF) polymer crystals.

The paper is outlined as follows. In Section II we present theory, including a formulation of stress calculations in spin vdW-DF, and a discussion of modeling phase stability in cases where XC calculations yield soft modes. Section III presents a number of challenges, from hard to soft, on which we validate the theory contribution and illustrate use of the consistent-vdW-DF tool chain: This section also presents the computational details as they pertain to our study of these challenges. Section IV and V present our results for hard and soft matter problems, respectively. Finally, Section VI contains a discussion and summary. The paper has one appendix.

II. THEORY

The vdW-DF method is in general well set up as a materials theory tool. It is, for example, implemented in broadly used DFT code packages such as QUANTUM ESPRESSO [41, 42], VASP [57, 58], WIEN2K [59, 60], CP2K [61, 62], as well as in GPAW [63, 64] and OCTOPUS [65–67] through our LIBVDWXC library [68]. The code packages come with a full set of vdW-DF versions and variants.

In some code packages the spin effects on energies, forces and stress are approximated by setting the nonlocal correlation terms without attention to spin impact on the underlying plasmon-dispersion model. This is not so in our full QUANTUM ESPRESSO implementation of spin vdW-DF (which includes spin versions of CX, CX0P, and AHCX), the implementation thus permits users to check if there are relevant spin vdW-DF effects to consider in their system of interest, for example, in the description of bulk cohesion [51]. However, to fully benefit from this QUANTUM ESPRESSO status, we need to enable variable-cell calculations by providing also a stress description for spin vdW-DF.

A. Spin vdW-DF calculations

The vdW-DF method is a systematic approach to design XC functionals that capture truly nonlocal correlation effects. Pure vdW interactions (produced by electrodynamic coupling of electron-hole pairs [22]) are examples of nonlocal-correlation effects. Another example is the screening (by itinerant valence electrons [22]) that shifts orbital energies as, for example, captured in a cumulant expansion. In the vdW-DF design we note that both are reflected in an electrodynamic reformulation of the XC functional. This allows us to treat all XC effects on the same footing in the electron-gas tradition.

In practice, we use a GGA-type functional $E_{\text{xc}}^{\text{in}}$ to define an effective (nonlocal) model of the frequency-dependence of the electron-gas susceptibility $\alpha(\omega)$. For

reasons discussed elsewhere [21, 35, 39], we limit this input to LDA plus a simple approximation for gradient-corrected exchange. We formally express the internal semilocal functional E_{xc}^{in} as the trace of a plasmon propagator $S_{xc}(\mathbf{r}, \mathbf{r}', \omega)$,

$$E_{xc}^{\text{in}} = \int_0^\infty \frac{du}{2\pi} \text{Tr}\{S_{xc}(\omega = iu)\} - E_{\text{self}}. \quad (1)$$

The trace is here taken over the spatial coordinates of S_{xc} . The term E_{self} denotes an infinite self-energy that removes the formal divergence.

The key point is that the model plasmon propagator S_{xc} also defines an effective GGA-level model dielectric function $\epsilon(iu) = \exp(S_{xc}(iu))$ and a corresponding model susceptibility $\alpha(iu) = (\epsilon(iu) - 1)/4\pi$. Moreover, by enforcing current conservation, the dielectrics modeling also defines the full vdW-DF specification of the XC functional,

$$E_{xc}^{\text{DF}} = \int_0^\infty \frac{du}{2\pi} \text{Tr}\{\ln(\nabla\epsilon_{xc}(iu) \cdot \nabla G)\} - E_{\text{self}}, \quad (2)$$

where G denotes the Coulomb Green function. By expanding Eq. (2) to first order in S_{xc} , one formally recoups the internal GGA-type functional Eq. (1). By further expanding to second order, we obtain the vdW-DF determination of corresponding nonlocal-correlation effects,

$$E_c^{\text{nl,sp}} = \int_0^\infty \frac{du}{4\pi} \text{Tr}\{S_{xc}^2 - (\nabla S_{xc} \cdot \nabla G)^2\}. \quad (3)$$

As indicated by superscript ‘sp’, the nonlocal-correlation term depends on the spatial variation in the spin polarization $\eta(\mathbf{r}) = [n_\uparrow(\mathbf{r}) - n_\downarrow(\mathbf{r})]/[n_\uparrow(\mathbf{r}) + n_\downarrow(\mathbf{r})]$.

Functionals of the vdW-DF family are generally expressed as

$$E_{xc}^{\text{vdW-DF}\#} = E_{xc}^0 + E_c^{\text{nl,sp}}, \quad (4)$$

where $E_{xc}^0 = E_{xc}^{\text{in}} + \delta E_x^0$ contains nothing but LDA and the gradient-corrected exchange. The $E_c^{\text{nl,sp}}$ is a correlation term. The Lindhard-Dyson screening logic formally mandates that the cross-over exchange term δE_x^0 must vanish, thus setting the balance between exchange and correlation. There are, however, practical limitations that prevent going directly for such fully consistent implementations directly. In the consistent-exchange vdW-DF-cx version we have chosen δE_x^0 so that the nonzero cross-over term does not affect binding energies, in typical bulk and in typical molecular-interaction cases, as discussed separately, Refs. 4, 22, 23, and 69.

For actual evaluations, we use a two-pole approximation for the shape of the plasmon-pole propagator S_{xc} . This plasmon-pole description, and hence the resulting vdW-DF version, is effectively set by the choice of the semilocal internal functional E_{xc} via Eq. (1). This leads to the computationally efficient nonlocal-correlation determination

$$E_c^{\text{nl}} = \frac{1}{2} \int_{\mathbf{r}} \int_{\mathbf{r}'} n(\mathbf{r}) n(\mathbf{r}') \Phi(D; q_0(\mathbf{r}); q_0(\mathbf{r}')), \quad (5)$$

where $D = |\mathbf{r} - \mathbf{r}'|$. It is given by a universal kernel form Φ , as discussed in Ref. 70. In Eq. (5), the values of $q_0(\mathbf{r})$ and $q_0(\mathbf{r}')$ characterize the model plasmon dispersion.

The above-summarized vdW-DF framework leaves no ambiguity about how to incorporate spin-polarization effects in $E_c^{\text{nl,sp}}$. Spin enters via the exchange and via the LDA-correlation parts of E_{xc}^{in} , as given by the spin-scaling description and by the now-standard PW92 formulation of LDA [71]. This, in turn, determines the form of S_{xc} and ultimately Eq. (5). Specifically, the values of $q_0(\mathbf{r})$ and $q_0(\mathbf{r}')$ are set from the local energy density of the internal semi-local functional to reflect the density and spin impact on the underlying screening description. Of course, it is imperative to also include spin in the term E_{xc}^0 .

B. The nonlocal-correlation stress tensor

For non-spin-polarized problems, there has since long existed a formulation of stress in vdW-DF calculation [72]. This allows effective KS structure optimizations as implemented in QUANTUM ESPRESSO. We now present a spin vdW-DF extension of stress to enhance the KS-structure search part. It is based on the ideas of Nielsen and Martin [73] and we first summarize the non-spin vdW-DF stress calculations, as derived by Sabatini and co-workers [72]. We consider the impact of unit-cell and coordinate scaling, for example, as expressed in cartesian coordinates for a position vector $r_\alpha \rightarrow \tilde{r}_\alpha = \sum_\beta (\delta_{\alpha,\beta} + \varepsilon_{\alpha,\beta}) r_\beta$, where $\varepsilon_{\alpha,\beta}$ is the strain tensor. This scaling affects the double Jacobian, the total-electron density $n(\mathbf{r}')$, the total-density gradient $\nabla n(\mathbf{r})$ and the coordinate-separation variable D inside Φ in Eq. (5). Details of these differential scaling effects are discussed in Appendix A for the spin-polarized case.

In the absence of spin polarization, Sabatini and co-workers [72] derived the nonlocal-correlation stress tensor contribution

$$\begin{aligned} \sigma_{c,\alpha,\beta}^{\text{nl}} = & \delta_{\alpha,\beta} \left[2E_c^{\text{nl}} - \int n(\mathbf{r}) v_c^{\text{nl}}(\mathbf{r}) \right] \\ & + \frac{1}{2} \int_{\mathbf{r}} \int_{\mathbf{r}'} n(\mathbf{r}) n(\mathbf{r}') \frac{\partial \Phi}{\partial D} C_{\alpha,\beta}(\mathbf{r}, \mathbf{r}') \\ & - \int_{\mathbf{r}} \int_{\mathbf{r}'} n(\mathbf{r}) n(\mathbf{r}') \frac{\partial \Phi}{\partial q_0} G_{\alpha,\beta}(\mathbf{r}), \end{aligned} \quad (6)$$

where

$$C_{\alpha,\beta}(\mathbf{r}, \mathbf{r}') = (r_\alpha - r'_\alpha)(r_\beta - r'_\beta)/D, \quad (7)$$

and

$$G_{\alpha,\beta}(\mathbf{r}) = \frac{\partial q_0(\mathbf{r})}{\partial |\nabla n(\mathbf{r})|} \frac{(\partial n(\mathbf{r})/\partial r_\alpha)(\partial n(\mathbf{r})/\partial r_\beta)}{|\nabla n(\mathbf{r})|}. \quad (8)$$

This stress component is in part given by the nonlocal-correlation contributions, $v_c^{\text{nl}}(\mathbf{r})$ and E_c^{nl} , to the XC potential and XC energy. These contributions are given by

local values of an inverse length scale, $q_0(\mathbf{r})$, that determines the local plasmon dispersion. As such, the contributions depend on the density gradients and hence have an indirect dependence on coordinate scaling, as summarized in Eq. (8).

For actual evaluations it is important to note that the density gradient will scale in unit-cell and coordinates, both since the density scales with the unit-cell size and because the formal expression for the spatial gradient scales with coordinate dilation even at a fixed density. The former effect is incorporated by the term containing $v_c^{\text{nl}}(\mathbf{r})$. The latter effect is captured by the term in the last row of Eq. (6). Fortunately, the local variation of the inverse length scale q_0 is already computed as part of any self-consistent vdW-DF calculation.

The proper spin vdW-DF formulation is presently implemented in QUANTUM ESPRESSO, in WIEN2K and in our LIBVDWXC (and thus available also in both GPAW and OCTOPUS). For spin-carrying systems we generally work with the spin-up and spin-down density components $n_{s=\uparrow,\downarrow}(\mathbf{r})$ of the total electron density $n(\mathbf{r}) = n_{\uparrow}(\mathbf{r}) + n_{\downarrow}(\mathbf{r})$. The internal functional depends on the variation in the spin polarization $\eta(\mathbf{r})$ and this spin dependence impacts the plasmon dispersion, and ultimately $E_c^{\text{nl,sp}}$, through the local $q_0(\mathbf{r})$ values.

To also compute stresses in spin vdW-DF we must update Eq. (6) accordingly; Details are discussed in Appendix A. We find that the second line of Eq. (6) only changes to the extent that the values of the q_0 's must now be evaluated for $\eta(\mathbf{r}) \neq 0$. For the first line, there is a small modification since separate XC potentials now act on $n_{\uparrow}(\mathbf{r})$ and $n_{\downarrow}(\mathbf{r})$.

Finally, for an update of the third line of Eq. (6), we simply track the variation of the local q_0 values on both spin-density gradient terms. Thus, the resulting spin-vdW-DF stress tensor expression becomes

$$\begin{aligned} \sigma_{c,\alpha,\beta}^{\text{nl,sp}} = & \delta_{\alpha,\beta} \left[2E_c^{\text{nl}} - \sum_{s=\uparrow,\downarrow} \int n_s(\mathbf{r}) v_{c,s}^{\text{nl,sp}}(\mathbf{r}) \right] \\ & + \frac{1}{2} \int_{\mathbf{r}} \int_{\mathbf{r}'} n(\mathbf{r}) n(\mathbf{r}') \frac{\partial \Phi}{\partial D} C_{\alpha,\beta}(\mathbf{r}, \mathbf{r}') \\ & - \int_{\mathbf{r}} \int_{\mathbf{r}'} n(\mathbf{r}) n(\mathbf{r}') \frac{\partial \Phi}{\partial q_0} \sum_{s=\uparrow,\downarrow} G_{\alpha,\beta}^s(\mathbf{r}), \quad (9) \end{aligned}$$

where

$$G_{\alpha,\beta}^{s=\uparrow,\downarrow}(\mathbf{r}) = \frac{\partial q_0(\mathbf{r})}{\partial |\nabla n_s(\mathbf{r})|} \frac{(\partial n_s / \partial r_\alpha)(\partial n_s / \partial r_\beta)}{|\nabla n|}. \quad (10)$$

As in the non-spin-polarized case, the spin vdW-DF stress contribution, Eq. (10), is conveniently given by quantities that are already computed in a self-consistent determination of the electron density variation in spin vdW-DF.

Sabatini *et al.* [72] incorporated their non-spin result in

the QUANTUM ESPRESSO package, and we have implemented and released our here-described spin extension in the same package.

C. Hybrids based on GGA and vdW-DF

In total, eight different functionals were used for the calculations. In some perovskite studies we include results obtained by the local-density approximation (LDA) [71] for reference. For studies with density-explicit GGA and vdW-DF, we generally rely on the PBE [30] and CX [4, 23] versions; For polymers we also compare CX results to vdW-DF1 [16] and vdW-DF2 [36] results.

For some hard and soft systems, we use and compare results obtained in PBE- and CX-associated hybrids, both unscreened and in a RSH form. The vdW-DF-cx0 class is an unscreened hybrid class that is formulated in analogy with the PBE0 [9, 11, 13]. We use the zero-parameter form CX0P [14] in which the extent of Fock exchange mixing is kept fixed at 20%, following an analysis of the CX coupling-constant scaling [40] that enters the general hybrid design logic [11, 14].

The HSE functional [12, 31] is a RSH extension of the PBE functional. We use it with 25% Fock exchange and a range separation that is described by a screening parameter $\mu = 0.2 \text{ \AA}^{-1}$. This parameter defines an error-function weighting $\text{erf}(\mu r)/r$ of the Coulomb interaction [12], thus limiting the Fock-exchange inclusion to short separations.

Finally, we have also used the recently launched CX-based RSH, termed AHCX [38], for a study of magnetic element structure and cohesion, as well as for some molecular benchmark studies. It resembles the CX0P in that we keep the Fock exchange fraction fixed at 20% and it resembles HSE in that we keep the screening parameter fixed at the standard HSE value [31]. The screening makes the AHCX calculations relevant for metallic systems [38].

D. Navigating phase transformations

Hard and soft matter come in different crystal forms, as well as meta-stable variants, and there is often a need for a concerted theory-experiment analysis to resolve and understand phase stability. This is true, for example, even in simpler (compact-unit-cell and nonmagnetic) perovskites [52, 53, 74–91] and in both nonpolar and ferroelectric polymers [92–105]. The structural transformations may be driven by temperature, electric fields, or strain; There can also be a release from meta-stable states that may have been locked in under synthesis or produced by usage [103].

First-principle calculations (that also accurately determine stress) may help in the analysis with volume-

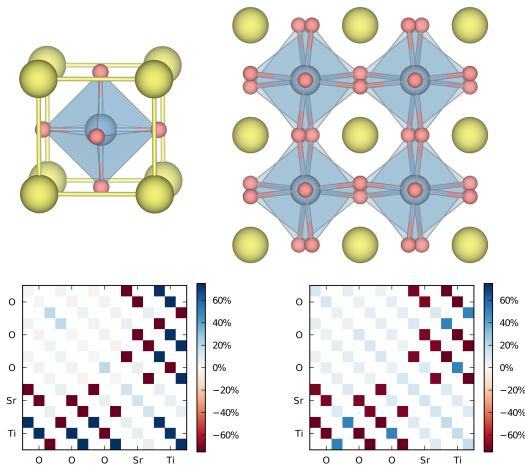


Figure 1. Top row depicts the conventional unit cell of SrTiO₃ (left) and a 40-atom cell (being a $2 \times 2 \times 2$ repetition) model that illustrates the oxygen dynamics in an important vibrational excitation at the R point of the Brillouin zone, involving rigid rotations of the oxygen octahedra. This is the AFD mode, experimentally known to drive a phase-transition below 105 K. The bottom row shows a comparison of relative changes in the dynamical matrix (evaluated at the Γ point) when going from PBE and to CX (left) and from CX to CX0P (right) for SrTiO₃.

constrained variable-cell calculations and by determination of the phonon spectra, as well as calculations of magnetic, elastic, polarization, and strain response [87, 90, 91, 103, 105–115]. For a given XC functional, we can rely on the Born-Oppenheimer (BO) approximation to determine what we call the native structure. This approach allows us to track the dependence of, for example, the BaZrO₃ form as a function of volume or pressure [53]. We can also compute the phonon spectra at the native structure or at the experimental structure and, for example, check for soft modes [52, 53]. Such first principle calculations help us identify the nature of a potential or actual instability, for example, when the cubic-system anti-ferrodistortive (AFD) mode is a potential driver for structural transformations [52, 53].

Similarly, we may for polymer crystals track the deformation that arises with electric fields [96] or with applied strain [103]. Here again first-principle calculations can identify not only the nature of modes and displacements, leading to a potential instability [102, 103], but also quantify the energy landscape for individual-strain or crystal transformations [103].

However, some effective modeling beyond the first principle calculations of structure and modes is still critically needed. This is because the finding of an imaginary frequency simply says that – for the chosen XC functional – there is an incipient instability; Treatments of zero-temperature and temporal fluctuations (correcting the underlying BO description) are essential to assert if

that XC functional predicts an actual phase transformation [85, 90, 91] or facilitates a polymer breakdown of long-range phase order [103]. For the simpler, compact-structure perovskites (like SrTiO₃), there exists both Monte-Carlo simulation frameworks [81, 83, 85, 88] and a phonon Green function formulation [90, 91], but something simpler is, in general, desirable to limit the computational load in complex systems.

E. Vibrations and stability: A simple analysis

Here, we illustrate use of a model analysis of quantum effects on transformations. The approach is generic to stability problems. Our model is inspired by a quantum theory of fluctuations above the phase-transition temperature [43]. Our analysis checks, for a given choice of XC functional, whether a DFT finding of a soft mode also implies the likely prediction of an actual transformation at $T \rightarrow 0$. Our modeling approach supplements the temperature-variation focus of Ref. 43 by also taking tunneling-induced vibrational-mode-level splitting into account. We focus the discussion on the SrTiO₃ AFD mode, and compare DFT characterizations obtained for a string of XC functionals.

The top right panel of Fig. 1 shows schematics of the SrTiO₃ atomic configuration in its cubic, high-temperature form; The top right panel illustrates the AFD mode, with compensating oxygen (red spheres) rotations. This mode causes a phase transition out of the cubic phase at 105 K in SrTiO₃; This phase transition does not occur in the similar BaZrO₃ systems [52, 53]. The mode is located at the R position of the Brillouin zone of the simple-cubic SrTiO₃ form [116]. It competes in SrTiO₃ with a Γ -point ferroelectric-instability mode that involves shifts of the Sr atoms (yellow spheres), but the R mode instability is experimentally known to suppress the latter instability [82, 85, 88, 91].

The bottom row of Fig. 1 emphasizes a general motivation factor for testing our CX/CX0P/AHCX tool chain on perovskites in general and for SrTiO₃ and BaZrO₃ in particular [52, 53]. The point is that the description of the interatomic forces (defining both the Γ - and R -mode phonons) differs significantly as we change between a choice of PBE-CX and CX-CX0P XC functionals. Specifically, the bottom-right panel lists, in color coding for all atom pairs (and the cartesian coordinates of the resulting forces, i.e., 15 by 15 entries in total) the relative change in forces as we go from CX to CX0P. A similarly large impact of the XC functional nature was previously documented for BaZrO₃, cf. Fig. 4 of Ref. 53. The differences (that affect the description of vibrations) exist even if all functionals accurately predict the cubic lattice constant.

The important step in a simple DFT-based stability modeling is to set up a size-consistent description of the vibrational mode that may drive distortions, for example, of

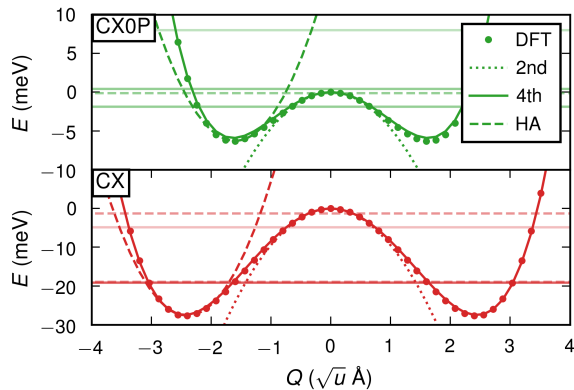


Figure 2. Potential energy landscape along a distortion coordinate Q representing the R_{25} phonon mode, as computed and modeled with CX0P (top panel) and CX (bottom panel). The solid curves show a 4th order fit to frozen-structure DFT results (marked with large dots) obtained for deformations in the range $Q \in [-3, 3] \text{ \AA}\sqrt{u}$ for a 40-atom cell. The dotted and dashed parabolaes show 2nd-order fits to the three data points (having atomic displacements of 0.01 \AA) closest to $Q = 0$ and for the displaced minima, denoted Q_0 ($Q_0 \approx -2.5 \text{ \AA}\sqrt{u}$ for CX): The latter is discussed as the harmonic approximation (HA) and it reflects the dynamics if the specific XC functional corresponds to a prediction of an actual low-temperature transformation. The solid and dashed horizontal lines indicate the energy levels obtained from the numeric solution to Eq. (11) as described in the full deformation and in the HA potentials, respectively.

the oxygen dynamics in the AFD mode in SrTiO_3 . The Hamiltonian for the ionic motion (in the BO approximation) in generalised canonical coordinates (denoted $Q_{s\mathbf{q}}$), can be written

$$H = T + V = \frac{1}{2} \sum_{s\mathbf{q}} \dot{Q}_{s\mathbf{q}} \dot{Q}_{s\mathbf{q}}^* + V, \quad (11)$$

The band index is s , and \mathbf{q} denotes the phonon momentum. The set of $Q_{s\mathbf{q}}$'s reflect the atomic displacements $\mathbf{d}_{s\mathbf{q}}^n$ and the phonon eigenvector $\mathbf{v}_{s\mathbf{q}}^n$ through the relation

$$\mathbf{d}_{s\mathbf{q}}^{n,\eta} = \frac{1}{\sqrt{\mathcal{N}M_n}} \sum_{s\mathbf{q}} Q_{s\mathbf{q}} \mathbf{v}_{s\mathbf{q}}^{n,\eta} e^{i\mathbf{q}\cdot\mathbf{R}_n}, \quad (12)$$

where η denotes the cartesian coordinate. Here \mathcal{N} is the number of assumed Born-von Karman repetitions, while \mathbf{R}_n and M_n denote the position and mass of the n 'th atom in the unit cell. For studying the stability of the AFD mode in the cubic structure only the momentum at the R point is needed. Also, as illustrated in Fig. 1, the AFD modes exclusively express oxygen rotations, leaving only oxygen-related terms in (12). Thus we can set $M_n = M \equiv 15.999$ atomic mass units (which we denote u).

For a non-interacting single- R -phonon mode, the potential energy variation can be approximated to the fourth

order in the AFD displacement d , or equivalently in the canonical coordinate in the specific mode, Q [44]. The resulting Landau expansion is

$$T + V = \frac{1}{2} \dot{Q}^2 + \frac{1}{2} \bar{\kappa} Q^2 + \frac{1}{4\mathcal{N}} \bar{\alpha} Q^4. \quad (13)$$

Here, $\bar{\kappa}$ and $\bar{\alpha}$ are effective material-specific constants of the Landau expansion for the AFD mode, reflecting both the effective interatomic couplings and inertia of the atoms involved in the dynamics [44]. The overbar is used to distinguish these parameters from those characterizing a (related) expansion the potential energy surface (PES) expressed in terms of AFD-type distortions (here denoted d) [52, 53], rather than phonon-mode coordinate Q .

The top (bottom) panel of Fig. 2 shows CX0P (CX) results for the total energy variation that occurs in SrTiO_3 when we track the AFD-type distortion (upper right panel of Fig. 1) while keeping the unit-cell lattice constants fixed at the optimal CX0P (CX) value. The dots show DFT results for the associated deformation energy as obtained for a 40 atom cell. The parameters $\bar{\kappa}$ and $\bar{\alpha}$ characterizing a fourth-order fit (solid curve) to the computed potential variations are presented in the result section IV.A. (in Table I).

For our parameter fittings, we note that Fig. 2 shows the total-energy variation (in a single cell of 40 atoms) as a function of the scaled AFD mode coordinate Q . The AFD mode in SrTiO_3 exclusively involves 16 identical oxygen and the same values, denoted d and v , define the magnitudes of the relevant oxygen displacements d and the relevant eigenvector components v . Normalization mandates that $v^2 = 1/16$ and, in this simplified description, Eq. (12) formally reduces to $Q = \sqrt{M\mathcal{N}}d/v$. We use $\mathcal{N} = 1$ for defining the coordinate scaling Q , as we fit $\bar{\kappa}$ and $\bar{\alpha}$ to the 40-atom PES shown in Fig. 2. The relation among quadratic coefficients (κ and $\bar{\kappa}$) in the related PES expansions, $V \approx \kappa d^2/2 = \bar{\kappa} Q^2/2$, is $\bar{\kappa} = \kappa/16M$.

The potential energy in Eq. (13) scales properly with respect to the chosen size of the supercell or Born-von Karman representation, i.e., with \mathcal{N} . A doubling of the simulation cell in every direction ($\mathcal{N} \rightarrow 8\mathcal{N}$) yields the coordinate rescaling, $Q \rightarrow \sqrt{8}Q$, and the potential-energy rescaling

$$V = \frac{\bar{\kappa}}{2} Q^2 + \frac{\bar{\alpha}}{4\mathcal{N}} Q^4 \rightarrow 8 \frac{\bar{\kappa}}{2} Q^2 + \frac{\bar{\alpha}}{4 \cdot 8} 64 \cdot Q^4 = 8V. \quad (14)$$

Size consistency also holds for the kinetic-energy part and the set of solution vibrational frequencies, namely the phonon-type eigenlevels ω_i . These frequencies characterize the model dynamics Eq. (13) and they remain unchanged regardless of the choice of supercell size used in our DFT characterizations.

To provide a simple assessment of which functionals are consistent with an actual low-temperature transition (for a given material problem) we can compute (or measure) the potential-energy surface for deformations, for example, Fig. 2 (or Refs. 52 and 53), to thus set the Landau

description, Eq. (13). The second-order expansion parameter $\bar{\kappa}$ can sometimes (for example, in BaZrO₃) give a leading-order estimate, $\omega_{i=1} \approx \sqrt{\bar{\kappa}}$, but a description of the fourth-order expansion term $\bar{\alpha}$ is essential when $\bar{\kappa} < 0$ (as we shall document holds for SrTiO₃ in all here-investigated functional cases). We then have a potential or incipient instability and further analysis is required.

The panels of Fig. 2 also show the AFD-type eigenvalue modes that result from solving for modal eigenlevels ω_i in the SrTiO₃ Landau modeling based on CX0P and CX calculations. The dashed horizontal lines describe the model eigenstate under the assumption that the system is actually deformed and the AFD dynamics occurs as trapped in one of the two displaced harmonic oscillators described by $Q = \pm Q_0$ (as illustrated by a dashed parabola). The pair of solid horizontal lines – in each panel – show the eigenlevels for the AFD-modal dynamics as described under the assumption that there is no relevant dephasing of the modal double-well dynamics [46, 47, 49]. That is, this double-well eigenvalue description of the vibration is provided under the condition that the mode retains coherence and thus exists on both sides of the central barrier at $Q \sim 0$.

The computed value of the coefficient $\bar{\kappa}$ in the Landau expansion identifies the presence of an incipient instability for cubic SrTiO₃ (the configuration described by $Q = 0$) in all of the LDA, PBE, CX, HSE, and CX0p functionals. However, we must also consider the fourth-order term. The double-well shapes produce instead phonon-mode eigenvalues ω_i with a splitting, denoted 2Δ . The splitting is inversely related to the depth of the double well: It is very small for LDA, fairly large for CX0P and large for HSE. However, a negative $\bar{\kappa}$ value does not necessarily imply a prediction of an actual deformation.

To set up a simple stability criterion, we consider the SrTiO₃ (and general incipient-instability) case as an inelastic tunneling problem [46–50]. We use the modal splitting to define a characteristic dwell or tunneling time:

$$\tau_R = \hbar/\Delta E. \quad (15)$$

We compare with an assumed inelastic-scattering or dephasing time τ_{scat} . A crude indicator for having a $T \rightarrow 0$ phase transition is

$$\tau_R \gg \tau_{\text{scat}}. \quad (16)$$

In essence, this is a competition between the phase-coherence life time and the tunneling dynamics of the mode that could possibly drive a transformation.

We motivate the stability condition Eq. (16) as follows: Tunneling, as well as thermally activated fluctuations, will connect the dynamics in both wells. The tunneling might be so slow that dephasing scattering occurs, preventing the mode from maintaining the coherence

that exists in an isolated quantum-mechanical double-well problem. In that case the inter-well dynamics is instead exclusively caused by thermal activation and there will (at $T = 0$) be a lock in into one of the wells. We interpret this lock-in as corresponding to an actual low-temperature transformation as $T \rightarrow 0$, and such transformation occurs in an LDA description of SrTiO₃ and BaZrO₃. It will also happen in CX, but it is not a result that emerges in our CX0P study of SrTiO₃ (as detailed below). The CX0P does have a soft mode at R and hence it predicts an incipient transition. However, the characteristic tunneling time (predicted in Section IV.A) suggests that dephasing is too slow to inhibit tunneling in the $T \rightarrow 0$ limit. In a CX0P-based description, we expect that tunneling prevents an actual low-temperature phase transformation.

The overall idea is perhaps best illustrated by an analogy to first-principle-theory-based analysis of addimer diffusion on metals, a problem that also provide a measured estimate for $\tau_{\text{scat}} \sim 1$ ps [117]. In the adatom/addimer-diffusion problems, for example, explored in Refs. 118–124, the dynamics eventually rolls over to a tunneling regime [120]. A scanning-tunneling microscopy study documents that the addimer dynamics will never freeze out [117]. The roll over to quantum-tunneling transport occurs below $T_{\text{cross}} = 5$ K, corresponding to $k_B T_{\text{cross}} \approx 1$ meV. This energy scale sets the time scale for $\tau_{\text{scat}} = \hbar/k_B T_{\text{cross}} \approx 0.7$ ps. The low-temperature dynamics of Cu(111) addimers can not be seen as thermally activated hopping between sites, i.e., the type of hopping (between dynamics in local wells) that eventually gets stuck in one or the other configuration. Rather, the dynamics maintains phase coherence and no actual lock in or trapping occurs [117, 120].

Our stability estimate Eq. (16) explains CX0P and CX stability differences, Section IV.A. It predicts that for CX0P-based (for CX-based) modeling of SrTiO₃, a tunneling regime will emerge (will not be relevant) at $T \rightarrow 0$. This means that the computed imaginary frequency value of the AFD mode is unlikely (likely) to drive an actual low-temperature transition in a CX0P (CX) characterization of SrTiO₃.

III. MATERIAL CHALLENGES AND COMPUTATIONAL DETAILS

Our results are obtained using both the (stress-updated) QUANTUM ESPRESSO DFT-code package [41, 42] and VASP with the setup of projector augmented wave potentials [57, 58]; Details are described as relevant in the subsections below. Ferroelectricity is a theme in our demonstrations and we use the modern (Berry-phase) theory of polarization [87, 106]. We rely on both the QUANTUM ESPRESSO and VASP implementations [125–129], reflecting code choices used for the specific hard and soft-matter problem.

A. SrTiO₃ properties

The problem of separating predictions of incipient and actual phase transitions motivates a detailed comparison of the tool-chain performance for SrTiO₃, as an illustration. Again, Fig. 1 shows the high-temperature cubic form, identifies the nature of the AFD distortion (as an R -mode instability, whether incipient or actual) and highlights that the CX-based XC tool chain yields significantly different descriptions of interatomic forces than what arises in PBE.

Our study also includes calculations of phonon frequencies and elastic coefficients and can in part be seen as an extension of a previous BaZrO₃ characterization [52, 53], by here looking at properties at the experimentally-observed lattice constant. However, since the SrTiO₃ is known to have an actual phase transition at 105 K, we cannot track the thermal impact on structure. Rather, we focus on discussing which functionals, if any, are consistent with this observation of a known SrTiO₃ instability, driven by the AFD mode.

Accordingly, we study the energy variations of a AFD-type distortion, as well as elastic-coefficients and high-frequency dielectric constants in BaZrO₃ and SrTiO₃, as illustrated in Fig. 1. To this end, we use the PAW method and the VASP [57, 58] software as well as PHONOPY [111] to determine the vibrational modes and frequencies in the cubic form, noting a need for additional modeling when the direct computation yields imaginary frequencies.

Our BaZrO₃ and SrTiO₃ studies are converged with respect to the wavefunction energy cut off. We have previously shown [53] that the AFD mode is very sensitive to the oxygen PAW potential and the energy cut-off, and thus we use the hard setup in VASP. For BaZrO₃ we use an energy cut-off of 1200 eV for LDA and GGA and 1600 eV for truly nonlocal functionals, i.e., HSE, CX, and CX0P. For SrTiO₃ energy cut-offs at 1600 eV are used for all functionals. Convergence turns out to be less sensitive to the k -point sampling and a $6 \times 6 \times 6$ Monkhorst-Pack [130] grid was deemed sufficient for the hybrid functionals, while $8 \times 8 \times 8$ was used for non-hybrid studies. The R_{25} and Γ_{15} frequencies were computed using the frozen phonon method with the default displacement of 0.01 Å in a 40 atom cell (being a $2 \times 2 \times 2$ repetition of the basic cell), and postprocessed in PHONOPY [111].

The one-dimensional PES were computed by mapping out the energy landscape along the R_{25} phonon mode, i.e., in a Glazer angle [131, 132] rotation around the z -axis, in steps of approximately 0.14 degrees. The energy levels were then obtained by solving the one-particle Schrödinger equation numerically in the potential given by the PES through the finite difference method.

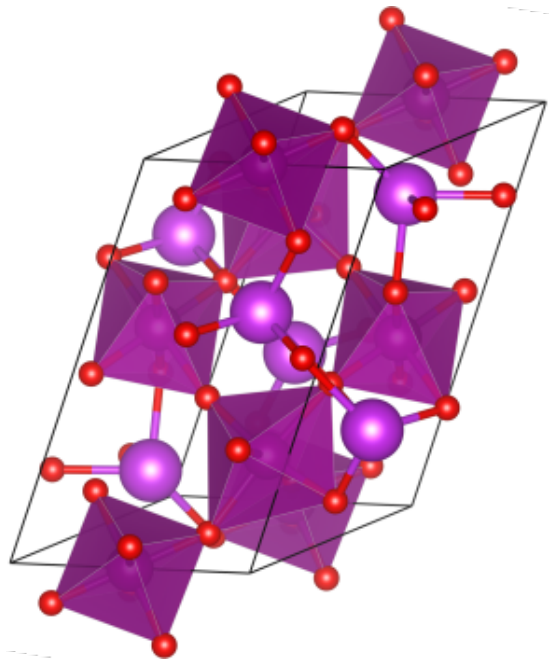


Figure 3. Primitive-cell representation of unit cell and atomic configuration in the magnetic perovskite BiMnO₃. The unit cell has a fairly large distortion of the cubic form with the basis plane (described by a and b lattice vectors) carrying almost all of the ferroelectric response. In our schematics of the atomic configuration we use red spheres to represent the O atoms and magenta spheres to represent the Mn atoms that carry ferromagnetic ordering. We also show the oxygen-octahedra that can be seen as encapsulating the Bi atoms.

B. Magnetic elements and perovskite

We can in general study bulk structure and compressibility properties of the magnetic Ni and Fe elements by mapping the bulk cohesive energy

$$E_{\text{coh}}(a) = E_{\text{bulk}}(a) - E_{\text{atom}} \quad (17)$$

as a function of the assumed lattice parameter a . To that end we provide and compare a set of PBE, CX, and AHCX calculations in our spin-stress updated version of QUANTUM ESPRESSO. We use optimized norm-conserving Vanderbilt [133] (ONCV) pseudopotentials (PPs) in the SG15-release [134]. For the AHCX Fe and Ni problems, we used a plane-wave cutoff at 200 Ry and a $10 \times 10 \times 10$ Monkhorst-Pack [130] k -point sampling, keeping contributions from all k -point differences in the Fock-exchange evaluation. We fit the results for the energy-versus-lattice constant variation to a fourth-order expansion [135], thus extracting the optimal lattice constant $a_{0,\text{fit}}$, cohesive energy $E_{\text{coh}}(a_{0,\text{fit}})$, and bulk modulus B_0 .

Variable-cell calculations involving a fraction of Fock exchange (as in hybrids) are flagged as incompletely tested in the QUANTUM ESPRESSO version that we used for the AHCX launch [38]; It is a question outside our focus on stress from nonlocal correlation and we limit variable-

cell structure determinations to CX. In principle, such calculations give us different lattice constants, denoted $a_{0,\text{stress}}$. We compare $a_{0,\text{stress}}$ and $a_{0,\text{fit}}$ for Ni and Fe to test and validate the spin-*vdW*-DF stress result and implementation.

Figure 3 shows schematics of the BiMnO_3 unit cell and atom configuration: O atoms (red) traps Bi atoms in octahedral cages in a distorted ordering, while the Mn atoms (magenta) carry the ferromagnetic ordering. The BiMnO_3 perovskite has a fairly large structural deformation and thus represents another good system for testing the new spin-*vdW*-DF stress implementation as well as the CX accuracy. For this problem we determined the structure in QUANTUM ESPRESSO variable-cell calculations using a plane-wave cutoff of 160 Ry and a $10 \times 10 \times 6$ Monkhorst-Pack grid [130] to sample the Brillouin zone.

C. Biochemistry testing and organic ferroelectrics

The study of DNA fragments and of their assembly from building blocks is a rich research field. It is a goal of the overall *vdW*-DF method and long-term research program to realize accurate computationally effective studies of structure, of defects and intercalation [136], of fluorescence-marker base substitutions [137, 138], as well as of molecular dynamics to determine the entropic effects [139]. All of these problems are interesting for biochemistry in their own right.

Meanwhile, there is potential health-technology benefit from realizing flexible materials (polymers) with a large polarization response [104]. One can, for example, envision incorporation in bandages to allow a simple electric detection of swelling associated with infection. Such indirect detection could reduce the need for traditional, periodic visual inspections. This idea, however, hinges on 1) The possibility of synthesizing a ferroelectric polymer with a sufficient per-monomer polarization response, and 2) Achieving a sufficient polymer crystal ordering so that the local response also serves to define a sufficiently large net electric-signal output (in connection with deformations). Consistent *vdW*-DF calculations cannot directly help synthesis, but they can predict the structure of perfect crystals and then assert if the ideal polarization response is sufficiently large, for any given soft-ferroelectrics candidate.

We shall illustrate this for the polyvinylidene fluoride (PVDF) system. However, since we need to predict both structure and response, we first provide method validation. Fortunately, the richness of the DNA and biochemistry field means that it offers many testing opportunities as we also seek a deeper account of polymer physics in technology and in general [92–98, 100, 102, 103, 105, 140–143]. In all this soft-matter testing and application work we use the ONCV-SG15 PPs [133, 134] at 160 Ry energy cutoff in QUANTUM ESPRESSO. We also ensure an

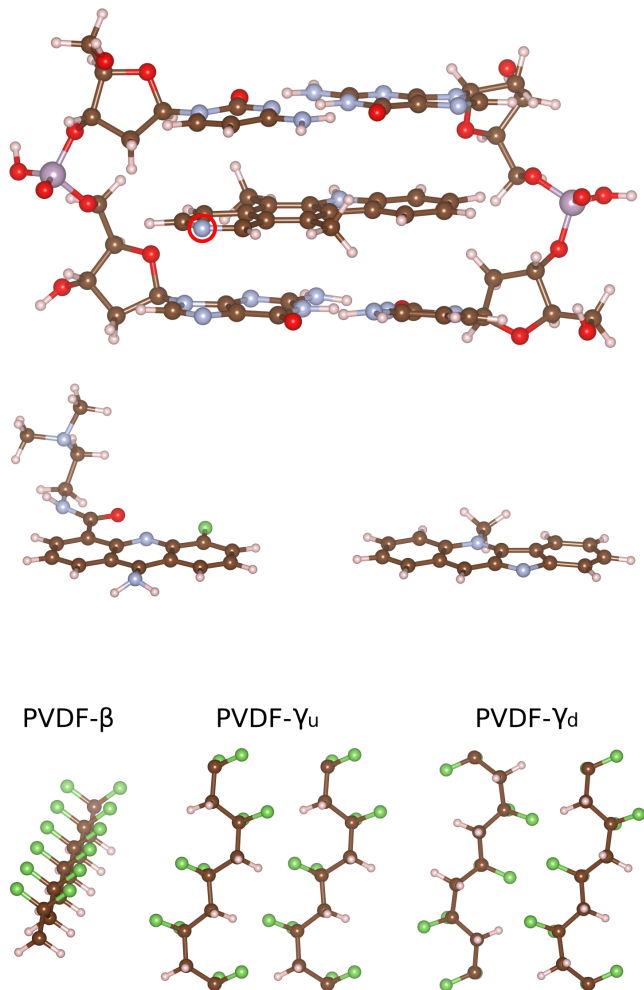


Figure 4. Structure model for DNA intercalation of the molecule with PDB code 1Z3F (also called ellipticine, top panel), alternative intercalants with PDB codes 1DL8 and 1K9G (the latter also called cryptolepine, middle panels), and the ferro-electric β as well as $\gamma_{u/d}$ forms of PVDFs (bottom row of panels). Brown, red, big/small blue, green, and white spheres identify C, O, P/N, F, and H atoms. Our CX tests are based on Ref. 136 reference geometries and CCSD(T) energies and we use their notation: The DNA-structure model shown in the top panel is denoted ‘B’ and involves a protonated backbone; There are also results for a model ‘A’ that omits the backbone. The intercalant in the top panel (1Z3F, henceforth denoted ‘3’) is also studied in a charged form ‘3⁺’ where a proton is added at the nitrogen identified by a red circle. The alternative intercalants shown in the middle left and right panels, 1DL8 and 1K9G, are denoted ‘2’ and ‘1’ respectively [136]. Finally, the PVDF forms (bottom row) are studied in crystals forms, see Figure 8 below, and Table VI.

electrostatic mono- and dipolar decoupling [144] in large cubic unit cells.

Figure 4 schematically shows a class of DNA intercalation problems (top and middle rows) that we use to validate accuracy of the consistent-exchange CX version before leveraging it on the application, the ferroelectric PVDF

polymer (bottom panel). In fact, we include two method-validation checks for soft-matter performance, namely a selection of benchmark sets from the GMTKN55 suite [145] and the DNA intercalation problems. Both focus on the CX energy description and thus supplement prior documentation of CX performance for structure and phonons in polyethylene and in oligoacene crystals [22, 54, 102, 103, 146].

The GMTKN55 is a suite of benchmarks of broad molecular properties that also contain a range of DNA-relevant benchmark sets. For a simple test of the CX, CX0P and AHCX performance on molecules it is relevant to consider the S66 set within the GMTKN55 suite [145]. It is a set that broadly reflects noncovalent interactions. More biochemistry-focused checks can be extracted by also computing mean-absolute deviations of our XC functional descriptions (relative to coupled-cluster CCSD(T) values [145]) for the PCONF21 set of peptide conformers, the Amino20x4 set of amino-acid interaction energies, the UPU23 set of RNA backbone conformer energies, the SCONF set of sugar conformers, and the WATER27 set. The testing setup is similar to what is used in Ref. 38 but here included also the WATER27 benchmarking set by computing the energy of the OH^- ion in a smaller 12 Å cubic cell. This allows us to circumvent adverse convergence impact of self-interaction errors [38, 147].

Additionally, we test by using a recent paper on DNA intercalation motifs [136]. The study identifies a set of relevant frozen coordinate geometries, Fig. 4, for which it also provides coupled cluster CCSD(T) reference energies. We use those energies for a test of the CX performance, because the model circumvents the need for a detailed study of the effects of counter ions and water.

The basic idea is to consider two models of a DNA base-pair segment, namely one where the backbone is protonated (effectively placing one extra electron per phosphor group on the back bone structure), and one where the back-bone is further eliminated. There are reference energies (and structures) for both models with 3 intercalants; In addition, there are also reference energies for a variant, where the intercalant is itself protonated.

For our soft-matter application study, we characterize primarily the β crystalline form of the PVDF system, while also comparing to the so-called γ forms, Fig. 4. We predict the relaxed structure and ferroelectric response of perfect crystals of β - and γ -PVDF, while comparing to experiments where possible. Both forms can be synthesized but, to the best of our knowledge, large single-crystal samples, with long-range order, do not yet exist. Theoretical predictions are thus motivated and we here seek to provide primarily a CX characterization in a $2 \times 2 \times 8$ Monkhorst-Pack grid sampling of the Brillouin zone.

We compute the polymer-crystal cohesive energy,

$$E_{\text{coh}}^{\text{pol}}(a, b, c) = E_{\text{crystal}} - 2E_{\text{monomer}} \quad (18)$$

for a series of unit-cell lattice constants in the β -PVDF form as well as for the motifs of the γ -PVDF form. Here again we use the stress-vdW-DF implementation in QUANTUM ESPRESSO. We also navigated the stiffness problem that results because variation in the polymer-direction c reflects variations in covalent bonds within a single PVDF strain, while variations in the a and b lattice constants reflect the noncovalent inter-polymer-strain bindings.

In practice, we proceed as follows for a characterization of the β phase. For a range of fixed c lattice-constant choices we optimize the structure using forces and stresses in a QUANTUM ESPRESSO variable-cell calculation that exclusively permits a and b structural relaxations. We then use a fourth-order polynomial fit to identify the minimum c_0 of the resulting $E_{\text{coh}}^{\text{pol}}(c_0, a(c_0), b(c_0))$ variation. This identifies the optimal structure as well as the actual crystal cohesion (in a given functional). The relaxation of PVDF in the γ -phase is carried out for the same PPs, but using a $2 \times 2 \times 8$ k -point grid.

Finally, an additional fourth order polynomial is used to define a contour plot of the $E_{\text{coh}}^{\text{pol}}(c_0, a, b)$ variation in the soft a and b unit-cell directions [102, 135, 142]. This is done to give a representation of the PES, noting that the c_0 -lattice constant exhibits only moderate changes with the XC functional choice. As such, this two-dimensional PES description offers us a chance to identify overall trends of functional impact on the PVDF characterization.

IV. HARD-MATTER EXAMPLES

A. Cubic perovskite properties and stability

Table I reports a summary of the BO characterizations of BaZrO_3 and SrTiO_3 as computed using LDA, PBE, CX, HSE, and CX0P. The top half of the table supplements our previous BaZrO_3 characterization [53] by here focusing on the impact that functional descriptions have on properties as described on the native BO lattice constants. This BaZrO_3 data also provides a reference for the SrTiO_3 characterizations that we include in the bottom half of the table.

For SrTiO_3 we find that LDA provides the best characterization of the high-frequency dielectric constant. For the elastic-constant description we find that it is CX and CX0P that delivers the most accurate description overall; The CX characterizations are helped by having an essentially perfect line up between the optimal CX BO lattice constant and experiments.

For the AFD R -mode and for the Γ modes of SrTiO_3 , we find soft modes for all functionals (except in the LDA- Γ_{15} description) in their description of the simple-cubic phase. Our PBE and HSE results for the soft Γ_{15} mode are in fair agreement with the values (PBE at $i14$ meV

Table I. Comparison of equilibrium lattice constant a (as obtained from a Birch-Murnaghan fit to DFT calculations in the BO approximation), frequencies of the lowest (and possibly soft) mode at the Γ - and R -point, Landau-model expansion parameters ($\bar{\kappa}$, $\bar{\alpha}$, see Eq. (13)), characteristic life-time (τ_R) of the phonon trapped in the double well potential, elastic coefficients, and the high-frequency dielectric constant ε_∞ . We list results computed in regular and hybrid functionals having either a semilocal- (PBE and HSE) or a truly nonlocal-correlation (CX and CX0P) description; LDA results and experimental values are included for reference. All results are obtained in a cubic cell at the native BO lattice constants a , except $\bar{\kappa}$, $\bar{\alpha}$ and τ_R which are obtained from the set of PES results, i.e., computed by deforming a 40-atom unit cell. Imaginary values in Γ_{15} or R_{25} reflect a possible or incipient instability in the description of the cubic cell by that functional. Corresponding identifier ‘*soft*’ in the experimental column reflects the observation of a low-temperature phase transition.

BaZrO₃	Exper.	LDA	PBE	CX	HSE	CX0P
a [Å]	4.188 ^a	4.160	4.237	4.200	4.200	4.183
Γ_{15} [meV]	15.2 ^b	13.04	11.97	13.70	13.47	14.85
R_{25} [meV]	5.9 ^a	<i>i</i> 7.17	2.30	<i>i</i> 2.53	6.12	5.49
$\bar{\kappa}$ [meV/Å ² u]	8.51 ^a	-12.5	1.27	-1.30	8.54	6.68
$\bar{\alpha}$ [meV/Å ⁴ u ²]	-	2.55	2.03	2.19	2.32	2.3
τ_R [10 ⁻¹² s]	-	6.0	-	-	-	-
C_{11} [GPa]	282/332 ^d	348	290	324	298	340
C_{12} [GPa]	88 ^c	88	79	89	84	87
C_{44} [GPa]	97/97 ^d	90	85	88	94	97
ε_∞	4.928 ^e	4.92	4.88	4.88	4.25	4.32
SrTiO₃	Exper.	LDA	PBE	CX	HSE	CX0P
a [Å]	3.905 ^f	3.862	3.942	3.905	3.900	3.880
Γ_{15} [meV]	<i>soft</i>	7.16	<i>i</i> 17.34	<i>i</i> 6.69	<i>i</i> 15.52	<i>i</i> 1.38
R_{25} [meV]	<i>soft</i>	<i>i</i> 11.15	<i>i</i> 8.34	<i>i</i> 8.88	<i>i</i> 3.29	<i>i</i> 5.56
$\bar{\kappa}$ [meV/Å ² u]	<i>soft</i>	-29.2	-16.3	-18.4	-3.8	-8.9
$\bar{\alpha}$ [meV/Å ⁴ u ²]	-	3.36	2.84	3.07	3.17	3.34
τ_R [10 ⁻¹² s]	-	14400	19	36	0.28	0.58
C_{11} [GPa]	318 ^g	381	314	348	361	337
C_{12} [GPa]	103 ^g	109	99	102	112	101
C_{44} [GPa]	124 ^g	118	111	115	128	123
ε_∞	-	6.34	6.335	6.30	5.076	5.202

^a Low temperature neutron measurements extrapolated to 0 K, Ref. 148

^b Ref. 149

^c Sound velocity measurements at 25°C, Ref. 150

^d Brillouin scattering at 93 K, Ref. 151

^e Ref. 152

^f High-resolution X-ray diffraction at room temperature, Ref. 153

^g Sound velocity measurements. Values extracted at 273 K, Ref. 154

and HSE at *i*9 meV) reported in Ref. 155, considering that we use a considerably larger energy cutoff.

The SrTiO₃ results for the R_{25} mode identify incipient instabilities, that is, they corresponds to possibilities for actual structural transformations, in all XC-functional cases. We recall that SrTiO₃ indeed undergoes an AFD-type transition to a tetragonal phase at 105 K [156], cor-

responding to compensating rotation of the oxygen cages, Fig. 1. Modeling based on a good XC functional should be consistent with this observation. Unlike the BaZrO₃ case, there are no low-temperature experimental data for the cubic phase but we can discuss the $T \rightarrow 0$ stability for would-be cubic SrTiO₃.

Fig. 5 shows calculations of the potentially unstable R AFD and Γ modes in cubic SrTiO₃ as a function of assumed lattice constants for the set of XC functionals LDA, PBE, CX, HSE, and CX0P. The figure reports frequency-square values, ω^2 (as computed in PHONOPY), reflecting a quadratic expansion in deformations in the cubic structure. The vertical dashed line shows the experimental lattice constant at room temperature while the dashed horizontal line is set at a zero- ω^2 value to delineate stability with a potential for instability. This is the measure that would apply if we could ignore zero-point energy dynamics of, for example, the AFD modes (for which the ω^2 values increase with the lattice constant). The large squares show the position of the optimal lattice constant for each functional. The set of curves shows the frequency-squared values ω^2 of the AFD R and of the ferroelectric-deformation Γ modes. These values are obtained in finite-difference PHONOPY calculations, for each of the functionals, as a function of the assumed cubic lattice constant.

We find that CX provides the best structural description in the sense that CX has both a highly accurate lattice constant description and that it’s predictions for the AFD phonon behavior is consistent with the experimentally observed SrTiO₃ phase transition, as argued in detail below.

On the one hand, the HSE delivers a description that is close on the lattice constant, but on the other, the HSE-based PHONOPY determination of the R -mode ω_R^2 value (at the optimal structure) is barely negative; Quantum fluctuations are expected to easily compensate this small potential for an AFD-driven phase transition. Worse, the HSE Γ -mode ω_Γ^2 value rapidly decreases beyond the BO lattice constant so that HSE instead suggests a ferroelectric SrTiO₃ behavior, again in conflict with observations.

Use of CX0P XC input gives ω_R^2 values which are more negative than those for HSE at the native CX0P lattice constant. It also yields a modal description with an improved resistance towards a Γ mode (ferroelectric) instability, Fig. 5. However, CX0P is still in conflict with experimental observations: When the CX0P input (for ω_R^2) is adjusted to the experimental lattice constant (vertical dashed line), it gives again only a very weak AFD-mode instability. Use of CX0P does not lead to the prediction of an actual low-temperature transformation in SrTiO₃. Still, it is interesting to contrast the CX0P stability analysis with that of CX.

Table I lists the parameters $\bar{\kappa}$ and $\bar{\alpha}$ that characterize the fourth-order fits to DFT results in the 5 functionals we use to model SrTiO₃. We note that large negative $\bar{\kappa}$

values correspond to deep double-well potentials which occur for LDA, CX (and to a similar extent for PBE). However, the total-energy variation (and hence the potential for the effective AFD-model Hamiltonian, Section II.D) is shallow for CX0P. We also note that the quality and the consistency of the Landau modeling (given by $\bar{\kappa}$ and $\bar{\alpha}$) is confirmed by checking the PHONOPY results, Table I, using the approximation $\omega_R^2 \approx \bar{\kappa}$.

In Table I we also list the tunneling times τ_R as extracted for the set of functionals, using Eq. (15). We find that LDA is characterized by very long (ns) dwell or tunneling times, while CX and PBE give moderately long times (36 and 19 ps). Finally, the table reports that CX0P and HSE are characterized by short dwell times (less than one ps). With an assumed dephasing time on the order of 1 ps, our simple stability model suggests that a CX (CX0P) description predicts (does not predict) an actual distortion at $T \rightarrow 0$.

In summary, we find that CX yields a better SrTiO₃ characterization than CX0P, when also considering the stability question. This is in contrast to the case of BaZrO₃, where CX0P performs better than CX for a broad study of properties. The perovskites is an example where more studies are needed to assert when we can systematically leverage hybrid advantages in combination with truly nonlocal correlations (as in CX0P and AHCX).

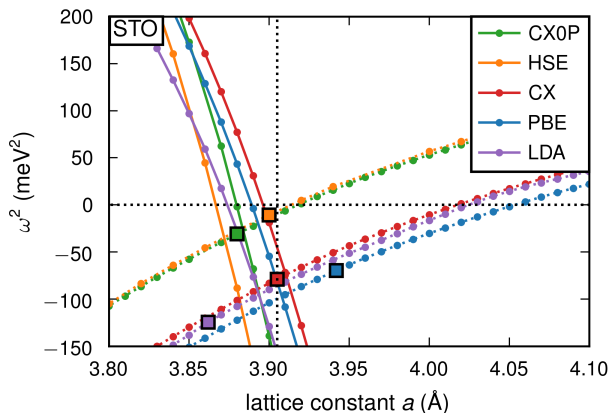


Figure 5. Evolution of the ferroelectric Γ_{15} mode (solid) and anti-ferrodistortive R_{25} mode (dashed) as function of lattice constant.

B. Magnetic elements and BiMnO₃

Figure 6 compares results in PBE, CX and AHCX for the cohesive energy for Ni (left column) and Fe (right column). The panels track the overall cohesive energy variation with the lattice constants a to identify the optimal native BO structure and associated cohesive energy for these magnetic elements. We compute sets of (PBE as well as) CX and AHCX cohesive energy val-

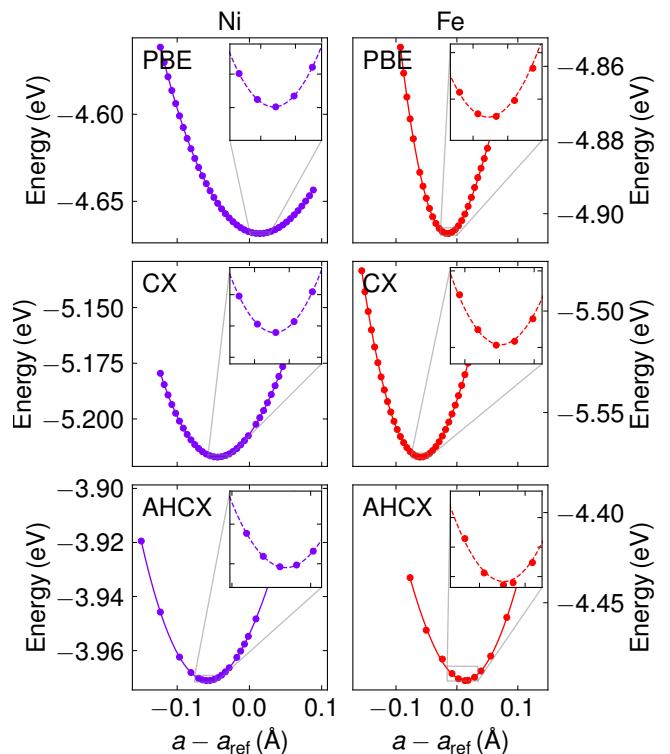


Figure 6. Cohesive-energy variation with lattice constant for Ni and Fe; See Table II for a summary of bulk structure characterization. The dots are the calculated values, the line is a fitting to a fourth order polynomial, Ref. 135. The curves are plotted relative to the experimental lattice constant a_{ref} , back-corrected for zero-point and thermal vibrational energy effects.

Table II. Structure properties of magnetic elements Ni and Fe obtained in spin-vdW-DF stress calculations, where practical, and checked by the polynomial fitting. The table compares for PBE, vdW-DF-cx and the associated range-separated vdW-DF-ahcx hybrid, the lattice constant a_0 , cohesive energy E_{coh} and bulk modulus B_0 against back-corrected experimental values, i.e., adjusted for zero-point and thermal vibrational lattice effects.

	PBE	CX	AHCX	Exper.* ^a
Ni				
$a_{0,\text{fit}}$ [Å]	3.524	3.466	3.452	3.510
$a_{0,\text{stress}}$ [Å]	3.524	3.466	–	
E_{coh} [eV]	4.668	5.217	3.971	4.477
B_0 [GPa]	197.0	226.3	227.1	192.5
Fe				
$a_{0,\text{fit}}$ [Å]	2.839	2.795	2.868	2.855
$a_{0,\text{stress}}$ [Å]	2.840	2.796	–	
E_{coh} [eV]	4.905	5.572	4.498	4.322
B_0 [GPa]	158.1	216.1	184.9	168.3

^a Ref. 157

ues at a set of frozen lattice constants a (dots) and we fit those energy variations to fourth-order polynomials (solid curves); The inserts validate the consistency of these fits (showing that they go through the computed minima). We compare our results for Ni and Fe to experimental values that have been back-corrected to account for zero-point energy and temperature vibrational effects. Our results and our approach yield both a comparison of CX and AHCX performance and an opportunity for a simple test of our new spin-vdW-DF stress description in the CX case.

In Table II we summarize the results of our magnetic-element structure characterizations. We see that while CX performs very well on structure and cohesion, across the set of nonmagnetic transition metals [51], it leads to a slight underestimation of the Ni lattice constants and a significant underestimation for Fe. However, we also find that the new AHCX partially corrects the Fe description.

Of direct interest for the here-presented theory and code work, Table II also shows that for CX (where we can use the spin-vdW-DF stress description in our updated QUANTUM ESPRESSO code), there is a near-perfect alignment of the variable-cell Fe and Ni descriptions and the results obtained through polynomial fitting for the minima, Fig. 6. We find our new spin-vdW-DF stress description validated.

Table III. Ground-state structure of the ferromagnetic and ferroelectric BiMnO₃. The volume Ω is reported per formula unit. For structure we compare to experiments at 20 K, Ref. 158. For the length of the polarization vector $|\mathbf{P}|$, we compare to experiments obtained at 5 K, Ref 159.

	CX	Exper.
a [Å]	9.49	9.52
b [Å]	5.57	5.59
c [Å]	9.62	9.84
α [°]	90.1	90.0
β [°]	109.3	110.6
γ [°]	91.62	90.0
Ω [Å ³]	59.93	61.40
$ \mathbf{P} $ [$\mu\text{C}/\text{cm}^2$]	36	23

Table III lists experimental observations on BiMnO₃, obtained using both X-ray diffraction and neutron diffraction at 5-300 K, [159]. The system has a ferromagnetic ordering. Accordingly, the data represents an additional route for us to illustrate use of the new spin-vdW-DF stress formulation, while also permitting a test of the accuracy of spin CX calculations.

We find that CX is accurate on the angles and side lengths, especially for the a and b lattice constants that define the basis plane in the schematics, Fig. 3. Accuracy in the description of this in-plane structure is important since this plane contains the main BiMnO₃ ferroelectric response. Overall, we find that the spin-vdW-DF stress description is both numerically stable and works in the

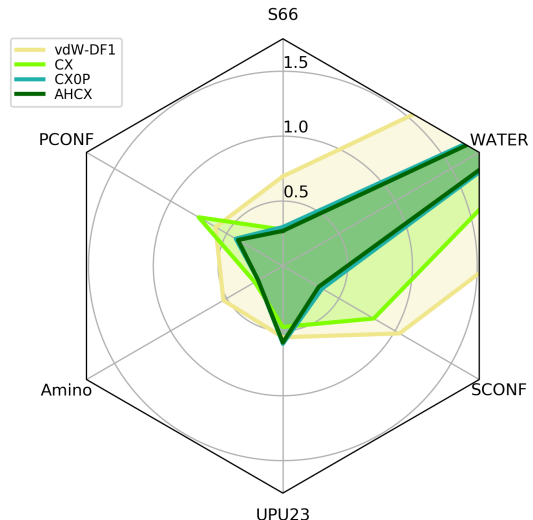


Figure 7. Performance assessment of the consistent-vdW-DF tool chain, CX-CX0P-AHCX, on 6 benchmark sets [145] of key bio-chemistry relevance, comparing relative molecule energies in: ‘S66’ (a balanced set), PCONF (tri- and tetrapeptide conformers), Amino20x4 (amino-acid conformers), UPU23 (RNA backbone conformers), SCONF (sugar conformers), and WATER27 (binding energies of water complexes, including some cases with proton transfers). We show mean-absolute deviation (MAD) values (expressed in kcal/mol) from quantum-chemistry CCSD(T) reference calculations [145], noting that performance of the unscreened hybrid CX0P (turquoise curve) is almost on par with that of the range-separated hybrid AHCX (dark green curve). We also include a performance overview of the original vdW-DF1 version [16, 34] that shares the nonlocal-correlation energy formulation. The WATER27 benchmarking on the consistent-vdW-DF tool chain yields slightly larger MAD values: 2.89, 2.84, and 2.80 kcal/mol for CX, CX0P, and AHCX).

sense that it reliably predicts an optimal structure even in more complex magnetic perovskite structure cases.

V. SOFT-MATTER EXAMPLES

A. DNA-related tests of vdW-DF-cx accuracy

Figure 7 shows a performance comparison for the CX-based consistent-vdW-DF tool chain, on a subset of benchmarks of the GMTKN55 suite that probes broad molecular properties. The benchmark sets were identified in Section III above and focus on bio-relevant problems, for example, peptides, RNA back bone, and sugar conformers (noting that sugar also defines the DNA back bone). The performance of the consistent-vdW-DFs (CX/CX0P/AHCX) is strong overall on molecules [38] and very strong for most of these bio-relevant problems. The performance is clearly better than, for example, that

Table IV. Comparison of CX intercalation energies, in kcal/mol, with CCSD(T), B3LYP-D3, and HF-3c results from Ref. [136]. All structures are computed at the experimentally motivated reference geometries, considering a double-basis set DNA-model without or with a (protonated) backbone, labeled ‘A’ and ‘B’, respectively [136]. The CCSD(T) reference energies exist for three intercalating molecules, here labeled ‘1’, ‘2’, and ‘3’, allowing also for a protonated molecule variant, denoted ‘3⁺’. The comparison with dispersion-corrected B3LYP results are for results obtained with the def2-TZVP basis set, using the Becke-Johnson damping function [160] on the semi-empirical Grimme-D3 correction term [145, 161]. The mean absolute deviations (MAD) from the CCSD(T)-calculations are given for CX, B3LYP-D3, and HF-3c.

System	CX	CCSD(T)	B3LYP-D3	HF-3c
1 A	-39.65	-41.99	-41.1	-40.3
2 A	-39.51	-39.52	-39.9	-35.7
3 A	-34.09	-34.57	-34.4	-32.4
3 ⁺ A	-47.04	-47.74	-47.9	-44.5
1 B	-43.60	-45.44	-45.2	-44.3
2 B	-45.25	-45.25	-45.7	-42.5
3 B	-39.86	-39.39	-40.2	-39.1
3 ⁺ B	-61.86	-62.55	-63.8	-61.6
MAD	0.82	-	0.54	2.00

of the original vdW-DF1 version [16, 34].

The WATER27 benchmark set constitutes a challenge for most XC functionals [22, 145]. Even here we find that the consistent-vdW-DF tool chain delivers a robust description, with a mean-absolute deviation (MAD) value of 2.8 kcal/mol for AHX and almost as good for the nonhybrid CX form. This suggests that CX and the tool chain is useful for determining interaction energies in biochemistry and, we expect, in both bio- and synthetic polymers. This positive test outcome substantiates previous results, finding a high CX accuracy for predicting the crystal structure of both oligoacene and polyethylene [102, 103, 146].

Table IV summarizes the additional CX benchmarking that we provide by studying intercalation energies for three nearly-planar molecules inserted into sections of DNA, as illustrated in the top and middle panels of Fig. 4. In Ref. 136 the atomic positions of the three intercalants, along with those of the immediate surrounding DNA structure, were extracted from the Protein Database (PDB) [162], and the interaction energies were calculated using the focal point approach [163] for extrapolated CCSD(T) results. We here use these CCSD(T)-extrapolated results as a benchmark. The structures used for the CCSD(T) results in Ref. [136] were truncated to the base pairs above and below the intercalant, plus the part of the sugar-phosphate backbone that connects them (model ‘B’, top panel of Fig. 4), or without the backbone (model ‘A’). Their models do not include solvent molecules or counter ions, and the backbones (model ‘B’) or the base pairs (model ‘A’) are passivated by pro-

tonation. The three intercalants have PDB codes 1K9G, 1DL8 and 1Z3F and are here (and in Ref. [136]) denoted ‘1’, ‘2’, and ‘3’ (see top and middle panels of Fig. 4). The latter molecule includes a nitrogen atom that can be protonated and this is also included in the set of calculations, the protonated molecule is denoted ‘3⁺’.

Table IV lists the interaction energies of molecules ‘1’, ‘2’, ‘3’, and ‘3⁺’ in DNA models ‘A’ and ‘B’, as calculated in Ref. [136] for CCSD(T), B3LYP-D3, and HF-3c, and calculated here using CX. All calculations are with atomic positions fixed to those extracted from PDB. Inspecting the numbers in Table IV, we see that CX yields results that are close to those from the CCSD(T) calculations, also for the protonated molecule (‘3⁺’). This holds whether the DNA backbone is included (model ‘B’) or not (model ‘A’). The largest deviation for CX is seen for molecule ‘1’ (in both DNA models), with a 1.8-2.4 kcal/mol difference from the CCSD(T)-energies. All other deviations are less than 0.7 kcal/mol, and MAD is 0.82 kcal/mol for CX with respect to CCSD(T). This can be compared to the B3LYP-D3 deviations from CCSD(T), that show a slightly smaller MAD (0.54 kcal/mol) on the set of intercalate structures. However, B3LYP-D3 (and HF-3c) are hybrid calculations, and in plane-wave codes molecular hybrid calculations are found to be up to 30 times slower compared to regular functionals, like CX, for similar system sizes [38].

Turning to the results for the minimal-basis method HF-3c [136] we see that the MAD value is more than double that of the CX results, at 2.00 kcal/mol. In other words, CX competes well with the best hybrid results of Ref. [136], and offers a path to acceleration that gives improved predictability compared to the HF-3c minimal-basis-set approach.

B. PVDF: a ferro-electric polymer crystal

Figure 8 shows an overview of the structure search and potential-energy landscape for deformations of β -PVDF that we have computed using CX (as well as in vdW-DF1 and vdW-DF2). The structure is obtained using a two-stage unit-cell relaxation scheme that handles the significant stiffness-anisotropy problem in PVDF and polymer crystals in general.

The figure also summarizes the results of this optimal-structure determination for β -PVDF. The intra-polymer bonds sets the optimal structure in c direction. These are of covalent nature and much stronger (with higher strain-energy) than the noncovalent inter-polymer bindings that govern the a and b lattice constants in the crystal. Accordingly we first pick a range of possible c lattice constants and proceed with variable-cell calculations that exclusive relaxes the a and b constants (as well as the atomic coordinates). This gives us the $E(c)$ shown in the left panel, from which we extract the optimal c_0

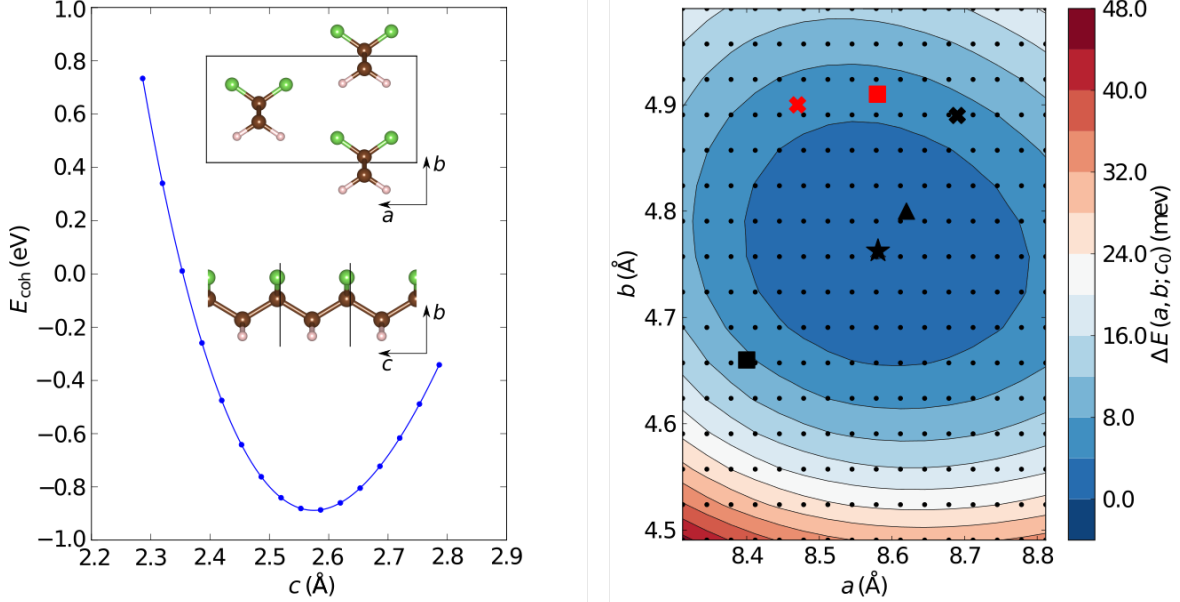


Figure 8. PVDF energy dependence on lattice parameters generated by a set of vdW-DF-cx calculations (dots). The left panel shows the cohesive energy for a constrained optimization, the right panel shows contours along a and b generated by a triangular mesh based on the interpolated relax calculations. The energy landscapes are given relative to the energy of the relaxed structure (marked by the star in right panel). The black triangle and square are the relaxed results using vdW-DF and vdW-DF2, respectively [105], while the black cross shows relaxed result for PBE0 [98]. The red cross shows the results from X-ray diffraction at 323 K [92] while the red square is X-ray diffraction from Ref. 93.

Table V. Calculated lattice parameters for the β -PVDF crystal. We compare with literature calculational results and room-temperature experiment data.

	a_0 [Å]	b_0 [Å]	c_0 [Å]	Ω [Å ³]
PBE0 ^a	8.64	4.82	2.64	109.2
PBE ^b	8.95	5.00	2.59	115.7
LDA ^b	7.97	4.46	2.56	90.2
vdW-DF1 ^b	8.62	4.80	2.60	107.5
vdW-DF2 ^b	8.40	4.66	2.60	101.8
vdW-DF1	8.61	4.79	2.60	107.1
vdW-DF2	8.38	4.67	2.59	101.5
CX, constrained fit	8.581	4.763	2.575	105.3
CX, vc-relax	8.585	4.745	2.575	104.9
X-ray diffraction ^c	8.47	4.90	2.56	106.2
X-ray diffraction ^d	8.58	4.91	2.56	107.8

^a Ref. 98

^b Ref. 105

^c Ref. 92

^d Ref. 93

lattice constant as well as the rest of the lattice constants and crystal cohesive energy.

The right panel of Fig. 8 shows an additional survey of the potential-energy variation that characterizes the crystal at the optimal c_0 value. This mapping is obtained for CX

by varying the a and b values and allowing for atomic relaxations. It is a fixed- c_0 projection of the ground-state energy variation. Furthermore, because the stiffness in the c direction is by far the highest in β -PVDF, this projection or PES gives an impression of the energy gradients that determine the lowest-lying vibrational excitations in the β -PVDF crystal.

Table V summarizes the CX structure characterization along with those obtained using vdW-DF1 and vdW-DF2 and those found in literature. The right panel of Fig. 8 provides an overview, using color symbols. We note that this is possible (even if the panel shows a potential-energy variation at the fixed optimal CX- c_0 value), because the XC functionals are in fair agreement on the c_0 value.

We find that CX results obtained with the above-described constrained-fit procedure align with those obtained in a constraint-free variable-cell optimization. However, that is true only when we start the system description of the polymer crystal close to the actual ground-state structure. In Table V we give an extra decimal in the reporting to facilitate this comparison.

We also find that CX provides a highly accurate prediction of the optimal c lattice constant for the β -form relative to experiments; That is, the description of unit-cell extension along the polymer chains is almost spot-on the experimental observation. In the other directions,

we find an overestimation of the a lattice constant but an underestimation of the b lattice constant. The PBE0 and vdW-DF1 results are in closer agreement with the b lattice constant but there the c lattice constant is significantly overestimated.

Table VI. Unit-cell lattice parameters for γ -phases of PVDF, obtained using full unit cell relaxations. The experimental values rely on a sample that contains a mixture of the up and down configurations, characterized at $T = 300$ K. The unit cell is nearly orthorhombic, with a small tilt of the along-strain axis c and the $a - b$ basis plane.

Functional	$a[\text{\AA}]$	$b[\text{\AA}]$	$c[\text{\AA}]$	$\Omega[\text{\AA}^3]$	$\angle ac[^\circ]$
γ_d Phase					
vdW-DF1	9.41	5.08	9.50	454.97	90.0
vdW-DF2	9.17	4.99	9.43	431.90	90.2
CX	9.31	5.02	9.60	449.28	90.0
γ_u Phase					
vdW-DF1	9.60	4.98	9.31	444.32	96.5
vdW-DF2	9.34	4.86	9.31	421.42	96.0
CX	9.36	4.84	9.32	421.81	94.6
Exper. ^a	9.67	4.96	9.20	440.65	93

^a Ref. 164

The study of the γ -PVDF crystal offers additional opportunities for a theory-experiment comparison. These crystal forms are only nearly orthorhombic, characterized by a tilt angle between the $a - b$ basis plane and the c axis that is (as for β -PVDF) aligned with the polymer strains. The comparison is complicated by the fact that there are two conformers, denoted γ_u and γ_d , see Fig. 4.

Table VII. Predictions of spontaneous polarisation of the three PVDF phases, studied using different vdW-DF releases. All the values are presented in the unit of $\mu\text{C cm}^{-2}$. It should be noted that experimental determination of the spontaneous polarization is hard as the samples are often mixtures of both various polymorphs and noncrystalline regions. Accordingly, the same experimental range is reported for both γ phases.

Phase	vdW-DF1	vdW-DF2	CX	Exper.
β	52.0	51.2	53.2	10^a
γ_u	9.5	7.2	7.7	$0.2 - 0.3^b$
γ_d	7.6	5.3	8.2	$0.2 - 0.3^b$

^a Ref. 95

^b Ref. 99

Table VI shows the results of a vdW-DF1, vdW-DF2, and CX structure characterization, along with experimental observations for γ -PVDF [164]. These reference values are obtained at room temperature in systems that are known to contain a mixture of the two motifs, i.e., both γ_u and γ_d . We note that one would expect the volume Ω , the tilt-angle, and the lengths of the set of unit-cell vectors to be a linear combination of γ_u and γ_d values. Moreover, polymers are known to exhibit a significant temperature expansion [146]; A good description should be smaller than the volume measured at 300 K.

We find that the computed structures for the γ_d motif differ from the room-temperature experimental characterization, for all vdW-DF functionals. The tilt angle differs and so does the predictions for the along-strain extension (length of c). The CX characterization of the γ_d motif is, overall, not as close to the measurement as vdW-DF2. We note that CX is often found accurate on covalent/metallic bonding and structure, Refs. [4, 22, 51, 54, 146] and that holds also for β -PVDF, Table V.

Assuming instead that the structure of the experimental sample is dominated by the γ_u motif, the set of vdW-DF predictions are closer to the data. Here, CX describes a unit-cell tilt angle that is in good agreement with the measurement. Also, both vdW-DF2 and CX are now found to give a unit-cell description that is 5% smaller than the room-temperature measurements and the CX lattice constant is now in good (1%) agreement with the measured c -axis extension.

Overall, the CX is found accurate on structure for β -PVDF and consistent with the mixed- γ -motif measurements. This, in turn, makes it relevant to use CX also for predicting and comparing the polymer ferroelectric response.

Table VII summarises this response survey. The polarization is computed using the Berry-phase approach [87, 106, 165]. This is done under the assumption of having a perfect crystal at the optimal structure (as computed for each of the vdW-DFs). We repeat that fully crystalline samples do not yet exist and that polarization measurements will be affected by compensating responses arising in different sample regions.

Hence, we provide these theoretical characterizations not as a performance assessment but as an application example. Polymer scientists cannot easily assert an upper limit on the polymer response from present PVDF measurements, but modern DFT can provide and compare, for example, among PVDF forms. Our CX calculations confirm that the β -PVDF form has the highest limit on the polarization response and may therefore eventually serve as a good organic ferroelectrics.

VI. DISCUSSION AND SUMMARY

An overall goal of this theory, code, validation and application paper was to illustrate potential materials-theory advantages of having a tool chain of related consistent-vdW-DF XC functionals, namely CX, CX0P, and the new AHCX. Our range-separated AHCX hybrid is very new but we have been able to include a few examples that nevertheless identify application strengths beyond those discussed in the AHCX launching work [38]. By providing a CX-based set of related XC tools, we have the option of including both truly nonlocal correlation and truly nonlocal exchange (to an increasing extent) all within the electron-gas tradition. As such it provides the

same advantages for vdW-dominated problems (and hard and soft matter in general) that the PBE-PBE0-HSE chain provides in the framework of semilocal-correlation descriptions. It provides a platform for developing a systematic analysis, as the consistent-vdW-DF application range grow.

More specific goals were to upgrade the proper spin vdW-DF formulation with a stress description and to illustrate a simple framework for understanding stability in a given DFT-based modeling. We sought the goals to facilitate modeling from hard to soft matter (inside our new XC tool chain). Here we have 1) Coded the spin-vdW-DF stress result in QUANTUM ESPRESSO to enable variable-cell vdW-DF calculations in spin systems and 2) used a simple stability condition to discuss soft modes in SrTiO₃, as an example. Having access to a simple, generic, stability gauge means that DFT practitioners have an option of seeking the most relevant DFT input (controlled by the XC choice) before proceeding with advanced modeling.

We have documented the spin-stress method contribution for magnetic elements as well as for a magnetic perovskite. In addition, we have also provided hard- and soft-matter illustrations of using the new tool chain of consistent-vdW-DF XC functionals on benchmarks, a new test of CX performance on DNA intercalation, and a ferroelectric-polymer application of the CX version.

Overall, we find that we will in general need more than just the CX part of the new nonlocal-correlation XC tool chain to cover materials from hard to soft. The AHCX improves the description of the magnetic Fe element over CX and both CX0P and AHCX are strong performers in our bio-relevant molecular benchmarking. However, hybrid vdW-DFs are not universally improving descriptions either, as discussed for SrTiO₃.

We present these results by looking at a number of hard and soft material cases, in the hope that they may stimulate further work and analysis. Studies using different – but closely related – regular/hybrid vdW-DFs are interesting not only because they do give useful results and, overall, accurate predictions. The closeness in the XC nature of our tool chain means that variations in performance may teach us to better weigh the balance (and screening) of truly nonlocal exchange in combination with our truly-nonlocal-correlation vdW-DF framework. We therefore intend to use of the consistent-vdW-DF tool chain more broadly to continue to gather performance statistics. Ultimately we aim to learn to better identify, *a priori*, the best DFT tool for a given material challenge.

ACKNOWLEDGEMENTS

We thank Göran Wahnström and Gerald D. Mahan for useful discussions. Work is supported by the

Swedish Research Council (VR) through Grants No. 2014-4310, 2016-04162, 2018-03964, and 2020-04997, the Swedish Foundation for Strategic research (SSF) through grants IMF17-0324 and SM17-0020, Sweden’s Innovation Agency (Vinnova) through project No.:2020-05179, as well as the Chalmers Area-of-Advance-Production theory activities and the Chalmers Excellence Initiative Nano. The authors also acknowledge computer allocations from the Swedish National Infrastructure for Computing (SNIC), under Contracts SNIC2019-1-12, SNIC2020-3-13, and from the Chalmers Centre for Computing, Science and Engineering (C3SE).

Appendix A: Coordinate transformations and stress

We consider small deformations, such that the displacements can be expressed in terms of the strain tensor $\varepsilon_{\alpha,\beta}$. This tensor describes coordinate transformations or scaling

$$\tilde{r}_\alpha = \sum_\beta (\delta_{\alpha,\beta} + \varepsilon_{\alpha,\beta}) r_\beta. \quad (\text{A1})$$

Here the subscripts, α or β , identify cartesian coordinates of the position vector \mathbf{r} . We seek to express the resulting stress that arises from the spin formulation $E_c^{\text{nl,sp}}$ of the nonlocal-correlation energy. This stress is formally given as a strain derivative

$$\sigma_{c,\alpha,\beta}^{\text{nl,sp}} \equiv -\frac{1}{V} \frac{\delta E_c^{\text{nl,sp}}}{\delta \varepsilon_{\alpha,\beta}}, \quad (\text{A2})$$

where V denotes the unit-cell volume.

We therefore aim to track every way that the coordinate scaling affects Eq. (5), for example, through the double spatial integrations, from the spin-density components $n_{s=\uparrow,\downarrow}(\mathbf{r})$, and from the kernel Φ dependence on coordinate separation D . We also need to track the stress that arises because the local inverse length scale $q_0(\mathbf{r})$ (inside Φ) depends on the spin-density gradients $\nabla n_{s=\uparrow,\downarrow}(\mathbf{r})$. These gradients change with coordinate scaling because scaling implies both a density change and a change in taking the derivative with positions. The approach is simply to apply the chain rule for derivatives with strain.

The transformation Jacobian is to lowest order

$$J = \left| \frac{d\tilde{\mathbf{r}}}{d\mathbf{r}} \right| = 1 + \sum_\alpha \varepsilon_{\alpha,\beta}, \quad (\text{A3})$$

and corresponds to the strain derivative $\partial J / \partial \varepsilon_{\alpha,\beta} = \delta_{\alpha,\beta}$. Since E_c^{nl} involves a double integration, this volume effect alone produces a the stress contribution $2E_c^{\text{nl}}\delta_{\alpha,\beta}$ in Eqs. (9) and (6).

The kernel Φ in Eq. (5) contains a term that depends explicitly on the separation D between two positions of the electron spin-density distributions. That term resembles the Hartree (or mean-field Coulomb) energy and

gives a stress component defined by the second row of Eq. (9) and Eq. (7). Of course, for the spin-polarized case, one must evaluate the kernel derivative $\partial\Phi/\partial D$ at inverse length scale values, $q_0(\mathbf{r})$ and $q_0(\mathbf{r}')$, for the actual spin-density distributions $n_{s=\uparrow,\downarrow}(\mathbf{r})$. However, that information is already available from any computations of the spin vdW-DF description of the nonlocal XC energy and XC potential.

In reciprocal space, the scaling is given by the transpose of $-\varepsilon_{\alpha,\beta}$. For example, a reciprocal lattice vector scales as

$$\tilde{G}_\alpha = \sum_\beta (\delta_{\alpha,\beta} - \varepsilon_{\beta,\alpha}) G_\beta. \quad (\text{A4})$$

It can readily be shown that with a planewave basis for wavefunctions $\Psi_{\mathbf{k},j} = \sum_{\mathbf{G}} c_{\mathbf{k}-\mathbf{G}}^{(j)} \exp(-i(\mathbf{k}-\mathbf{G})\cdot\mathbf{r})$ there are cancellations of strain effects in all but the normalization factors $c_{\mathbf{k}-\mathbf{G}}^{(j)}$. The spin-density components $n_{s=\uparrow,\downarrow}$ will therefore scale with derivatives given by the volume factor

$$\frac{\partial n_s(\mathbf{r})}{\partial \varepsilon_{\alpha,\beta}} = -\delta_{\alpha,\beta} n_s(\mathbf{r}). \quad (\text{A5})$$

However, following the logic of the original Nielsen and Martin analysis [73], the volume scaling of the densities can be summarized in terms of the relevant (spin-resolved) components $v_{c,s}^{\text{nl}} n_s(\mathbf{r})$ of the XC potential. The stress terms $-\delta_{\alpha,\beta} \sum_s v_{c,s}^{\text{nl}} n_s(\mathbf{r})$ in Eqs. (9) and (6) summarize all of the density-volume scaling effects for the spin-balanced and spin-polarized cases, respectively.

This finally brings us to the third row of Eq. (9). Here we capture the effects of strain scaling of the spin density gradient $\nabla n_s(\mathbf{r})$, assuming a fixed $n_s(\mathbf{r})$ variation:

$$\frac{\partial n_s(\mathbf{r})}{\partial r_\alpha} \rightarrow \frac{\partial n_s(\mathbf{r})}{\partial \tilde{r}_\alpha} \approx \frac{\partial n_s(\mathbf{r})}{\partial r_\alpha} - \sum_\beta \varepsilon_{\alpha,\beta} \frac{\partial n_s(\mathbf{r})}{\partial r_\beta}. \quad (\text{A6})$$

For the length of this derivatives we have

$$\frac{\partial |\nabla n_s(\mathbf{r})|}{\partial \varepsilon_{\alpha,\beta}} = -\frac{1}{|\nabla n_s(\mathbf{r})|} \frac{\partial n_s}{\partial r_\alpha} \frac{\partial n_s}{\partial r_\beta}, \quad (\text{A7})$$

because we have handled the volume scaling of the density separately [73]. The third row of the spin-vdW-DF stress description Eq. (9) follows by a simple application of the chain rule.

-
- [1] H. Rydberg, N. Jacobson, P. Hyldgaard, S. I. Simak, B. I. Lundqvist, and D. C. Langreth, *Hard numbers on soft matter*, *Surf. Sci.* **532–535**, 606 (2003).
- [2] D. C. Langreth, B. I. Lundqvist, S. D. Chakarova-Käck, V. R. Cooper, M. Dion, P. Hyldgaard, A. Kelkkanen, J. Kleis, L. Kong, S. Li, P. G. Moses, E. Murray, A. Puzder, H. Rydberg, E. Schröder, and T. Thonhauser, *A density functional for sparse matter*, *J. Phys.: Condens. Matter* **21**, 084203 (2009).
- [3] T. Björkman, A. Gulans, A. V. Krasheninnikov, and R. M. Nieminen, *Are we van der Waals ready?*, *J. Phys.: Condens. Matter* **24**, 424218 (2012).
- [4] K. Berland, C. A. Arter, V. R. Cooper, K. Lee, B. I. Lundqvist, E. Schröder, T. Thonhauser, and P. Hyldgaard, *van der Waals density functionals built upon the electron-gas tradition: Facing the challenge of competing interactions*, *J. Chem. Phys.* **140**, 18A539 (2014).
- [5] A. D. Becke, *Perspective: Fifty years of density-functional theory in chemical physics*, *J. Chem. Phys.* **140**, 18A301 (2014).
- [6] K. Burke, *Perspective on density functional theory*, *J. Chem. Phys.* **136**, 150901 (2012).
- [7] O. T. Hofmann, E. Zojer, L. Hörmann, A. Jeindi, and R. J. Maurer, *First-principles calculations of hybrid inorganic-organic interfaces: from state-of-the-art to best practice*, *Phys. Chem. Chem. Phys.*, *Advance Article* **23**, 8132 (2021).
- [8] A. D. Becke, *Density-functional thermochemistry. III. the role of exact exchange*, *J. Chem. Phys.* **98**, 5648 (1993).
- [9] C. Adamo and V. Barone, *Towards reliable density functional methods without adjustable parameters: The PBE0 model*, *J. Chem. Phys.* **110**, 6158 (1999).
- [10] J. P. Perdew, M. Ernzerhof, and K. Burke, *Rationale for mixing exact exchange with density functional approximations*, *J. Chem. Phys.* **105**, 9982 (1996).
- [11] K. Burke, M. Ernzerhof, and J. P. Perdew, *The adiabatic connection method: a non-empirical hybrid*, *Chem. Phys. Lett.* **265**, 115 (1997).
- [12] J. Heyd, G. E. Scuseria, and M. Ernzerhof, *Hybrid functionals based on a screened Coulomb potential*, *J. Chem. Phys.* **118**, 8207 (2003).
- [13] K. Berland, Y. Jiao, J.-H. Lee, T. Rangel, J. B. Neaton, and P. Hyldgaard, *Assessment of two hybrid van der Waals density functionals for covalent and noncovalent binding of molecules*, *J. Chem. Phys.* **146**, 234106 (2017).
- [14] Y. Jiao, E. Schröder, and P. Hyldgaard, *Extent of Fock-exchange mixing for a hybrid van der Waals density functional?*, *J. Chem. Phys.* **148**, 194115 (2018).
- [15] V. I. Anisimov, J. Zaanen, and O. K. Andersen, *Band theory and Mott insulators: Hubbard U instead of Stoner I*, *Phys. Rev. B* **44**, 943 (1991).
- [16] M. Dion, H. Rydberg, E. Schröder, D. C. Langreth, and B. I. Lundqvist, *Van der waals density functional for general geometries*, *Phys. Rev. Lett.* **92**, 246401 (2004).
- [17] E. R. Johnson, I. D. Mackie, and G. A. DiLabio, *Dispersion interactions in density-functional theory*, *J. Phys. Org. Chem.* **22**, 1127 (2009).
- [18] A. Tkatchenko, L. Romaner, O. T. Hofmann, E. Zojer, C. Ambrosch-Draxl, and M. Scheffler, *van der Waals interactions between organic adsorbates and at organic/inorganic interfaces*, *MRS Bulletin* **35**, 435 (2010).
- [19] S. Grimme, *Density functional theory with London dispersion corrections*, *WIREs: Comput. Mol. Sci.* **1**, 211

- (2011).
- [20] J. Klimeš and A. Michaelides, Perspective: Advances and challenges in treating van der Waals dispersion forces in density functional theory, *J. Chem. Phys.* **137**, 120901 (2012).
- [21] K. Berland, V. R. Cooper, K. Lee, E. Schröder, T. Thonhauser, P. Hyldgaard, and B. I. Lundqvist, van der Waals forces in density functional theory: A review of the vdW-DF method, *Rep. Prog. Phys.* **78**, 066501 (2015).
- [22] P. Hyldgaard, Y. Jiao, and V. Shukla, Screening nature of the van der Waals density functional method: A review and analysis of the many-body physics foundation, *J. Phys.: Condens. Matter* **32**, 393001 (2020).
- [23] K. Berland and P. Hyldgaard, Exchange functional that tests the robustness of the plasmon description of the van der Waals density functional, *Phys. Rev. B* **89**, 035412 (2014).
- [24] D. C. Langreth and J. P. Perdew, Theory of nonuniform electronic systems. I. Analysis of the gradient approximation and a generalization that works, *Phys. Rev. B* **21**, 5469 (1980).
- [25] D. C. Langreth and M. J. Mehl, Easily implementable nonlocal exchange-correlation energy functional, *Phys. Rev. Lett.* **47**, 446 (1981).
- [26] J. P. Perdew and Y. Wang, Accurate and simple density functional for the electronic exchange energy: Generalized gradient approximation, *Phys. Rev. B* **33**, 8800 (1986).
- [27] J. P. Perdew, K. Burke, and Y. Wang, Generalized gradient approximation for the exchange-correlation hole of a many-electron system, *Phys. Rev. B* **54**, 16533 (1996).
- [28] D. C. Langreth and S. H. Vosko, Exact electron-gas response functions at high density, *Phys. Rev. Lett.* **59**, 497 (1987).
- [29] D. C. Langreth and S. H. Vosko, Response functions and non-local functionals, *Adv. Quantum. Chem.* **21**, 175 (1990).
- [30] J. P. Perdew, K. Burke, and M. Ernzerhof, Generalized gradient approximation made simple, *Phys. Rev. Lett.* **77**, 3865 (1996).
- [31] J. Heyd, G. E. Scuseria, and M. Ernzerhof, Erratum: “Hybrid functionals based on a screened Coulomb potential” [*J. Chem. Phys.* 118, 8207 (2003)], *J. Chem. Phys.* **124**, 219906 (2006).
- [32] H. Rydberg, B. I. Lundqvist, D. C. Langreth, and M. Dion, Tractable nonlocal correlation density functionals for flat surfaces and slabs, *Phys. Rev. B* **62**, 6997 (2000).
- [33] H. Rydberg, M. Dion, N. Jacobson, E. Schröder, P. Hyldgaard, S. I. Simak, D. C. Langreth, and B. I. Lundqvist, van der Waals density functional for layered structures, *Phys. Rev. Lett.* **91**, 126402 (2003).
- [34] M. Dion, H. Rydberg, E. Schröder, D. C. Langreth, and B. I. Lundqvist, Erratum: Van der Waals Density Functional for General Geometries [*Phys. Rev. Lett.* **92**, 246401 (2004)], *Phys. Rev. Lett.* **95**, 109902 (2005).
- [35] T. Thonhauser, V. R. Cooper, S. Li, A. Puzder, P. Hyldgaard, and D. C. Langreth, van der Waals density functional: Self-consistent potential and the nature of the van der Waals bond, *Phys. Rev. B* **76**, 125112 (2007).
- [36] K. Lee, È. D. Murray, L. Kong, B. I. Lundqvist, and D. C. Langreth, Higher-accuracy van der Waals density functional, *Phys. Rev. B* **82**, 081101 (2010).
- [37] T. Thonhauser, S. Zuluaga, C. A. Arter, K. Berland, E. Schröder, and P. Hyldgaard, Spin signature of non-local correlation binding in metal-organic frameworks, *Phys. Rev. Lett.* **115**, 136402 (2015).
- [38] V. Shukla, C. Frostenson, Y. Jiao, and P. Hyldgaard, vdW-DF-ahcx: a range-separated van der Waals density functional hybrid, Submitted; <https://arxiv.org/abs/2105.02696> (2021).
- [39] P. Hyldgaard, K. Berland, and E. Schröder, Interpretation of van der Waals density functionals, *Phys. Rev. B* **90**, 075148 (2014).
- [40] Y. Jiao, E. Schröder, and P. Hyldgaard, Signature of van der Waals binding: A coupling-constant scaling analysis, *Phys. Rev. B* **97**, 085115 (2018).
- [41] P. Giannozzi, S. Baroni, N. Bonini, M. Calandra, R. Car, C. Cavazzoni, D. Ceresoli, G. L. Chiarotti, M. Cococcioni, I. Dabo, A. D. Corso, S. de Gironcoli, S. Fabris, G. Fratesi, R. Gebauer, U. Gerstmann, C. Gougoussis, A. Kokalj, M. Lazzeri, L. Martin-Samos, N. Marzari, F. Mauri, R. Mazzarello, S. Paolini, A. Pasquarello, L. Paulatto, C. Sbraccia, S. Scandolo, G. Sclauzero, A. P. Seitsonen, A. Smogunov, P. Umari, and R. M. Wentzcovitch, QUANTUM ESPRESSO: a modular and open-source software project for quantum simulations of materials, *J. Phys.: Condens. Matter* **21**, 395502 (2009).
- [42] P. Giannozzi, O. Andreussi, T. Brumme, O. Bunau, M. Buongiorno Nardelli, M. Calandra, R. Car, C. Cavazzoni, D. Ceresoli, M. Cococcioni, N. Collonna, I. Carnimeo, A. Dal Corso, S. de Gironcoli, P. Delugas, R. A. DiStasio Jr, A. Feretti, A. Floris, G. Fratesi, G. Fugallo, R. Gebauer, U. Gerstmann, F. Giustino, T. Gorni, J. Jia, M. Kawamura, H.-Y. Ko, A. Kokalj, E. Küçükbenli, M. Lazzeri, M. Marseli, N. Marzari, F. Mauri, N. L. Nguyen, H.-V. Nguyen, A. Otero-de-la Roza, L. Paulatto, S. Poncé, D. Rocca, R. Sabatini, B. Santra, M. Schlipf, A. Seitsonen, A. Smogunov, I. Timrov, T. Thonhauser, P. Umari, N. Vast, X. Wu, and S. Baroni, Advanced capabilities for materials modelling with Quantum Espresso, *J. Phys.: Condens. Matter* **29**, 465901 (2017).
- [43] G. D. Mahan, Quantum Theory of the Burns Temperature in Barium Titanate, *Journal of Electronic Materials* **42**, 2560 (2013).
- [44] J. Callaway, *Quantum Theory of the Solid State* (Academic Press, Inc. (London) LTD., Cambridge, United Kingdom, 1974).
- [45] L. L. Chang, L. Esaki, and R. Tsu, Resonant tunneling in semiconductor double barriers, *Appl. Phys. Lett.* **24**, 593 (1974).
- [46] S. Luryi, Frequency limit of double-barrier resonant-tunneling oscillators, *Appl. Phys. Lett.* **47**, 490 (1985).
- [47] M. Jonson and A. Grincwajg, Effect of inelastic scattering on resonant and sequential tunneling in double barrier heterostructures, *Appl. Phys. Lett.* **51**, 1729 (1987).
- [48] P. Hyldgaard and A. P. Jauho, Elastic and inelastic resonant tunneling in an imperfect superlattice, *J. Phys.: Condens Matter* **2**, L8725 (1990).
- [49] J. H. Davies, S. Hershfield, P. Hyldgaard, and J. W. Wilkins, Current and rate equation for resonant tunneling, *Phys. Rev. B* **47**, 4603 (1993).
- [50] P. Hyldgaard, S. Hershfield, J. H. Davies, and J. W.

- Wilkins, Resonant-tunneling with an electron-phonon interaction, *Annals of Physics* **236**, 1 (1994).
- [51] L. Gharaee, P. Erhart, and P. Hyldgaard, Finite-temperature properties of non-magnetic transition metals: Comparison of the performance of constraint-based semi and nonlocal functionals, *Phys. Rev. B* **95**, 085147 (2017).
- [52] E. J. Granhed, A. Lindman, C. Eklöf-Österberg, M. Karlsson, S. F. Parker, and G. Wahnström, Band vs. polaron: vibrational motion and chemical expansion of hydride ions as signatures for the electronic character in oxyhydride barium titanate, *J. Mater. Chem. A* **7**, 16211 (2019).
- [53] E. J. Granhed, G. Wahnström, and P. Hyldgaard, BaZrO₃ stability under pressure: the role of non-local exchange and correlation, *Phys. Rev. B* **101**, 224105 (2020).
- [54] F. Brown-Altwater, T. Rangel, and J. B. Neaton, *Ab initio* phonon dispersion in crystalline naphthalene using van der Waals density functionals, *Phys. Rev. B* **93**, 195206 (2016).
- [55] S. F. Yuk, K. C. Pitike, S. Nakhmanson, M. Eisenbach, Y. W. Li, and V. R. Cooper, Towards an accurate description of perovskite ferroelectrics: Exchange and correlation effects, *Nat. Sci. Rep.* **7**, 43482 (2017).
- [56] F. Jia, G. Kresse, C. Franchini, P. Liu, J. Wang, A. Stroppa, and W. Ren, Cubic and tetragonal perovskites from the random phase approximation, *Phys. Rev. Mat.* **3**, 103801 (2019).
- [57] G. Kresse and J. Furthmüller, Efficiency of *ab-initio* total energy calculations for metals and semiconductors using a plane-wave basis set, *Comput. Mater. Sci.* **6**, 15 (1996).
- [58] G. Kresse and J. Furthmüller, Efficient iterative schemes for *ab initio* total-energy calculations using a plane-wave basis set, *Phys. Rev. B* **54**, 11169 (1996).
- [59] P. Blaha, K. Schwarz, P. Sorantin, and S. Trickey, Full-potential, linearized augmented plane wave programs for crystalline systems, *Comp. Phys. Commun.* **59**, 399 (1990).
- [60] P. Blaha, K. Schwarz, F. Tran, R. Laskowski, G. K. H. Madsen, and L. D. Marks, WIEN2k: An APW+lo program for calculating the properties of solids, *J. Chem. Phys.* **152**, 074101 (2020).
- [61] J. VandeVondele, M. Krack, F. Mohamed, M. Parrinello, T. Chassaing, and J. Hutter, Quickstep: Fast and accurate density functional calculations using a mixed Gaussian and plane waves approach, *Comp. Phys. Commun.* **167**, 103 (2005).
- [62] T. D. Kühne, M. Iannuzzi, M. Del Ben, V. V. Rybkin, P. Seewald, F. Stein, T. Laino, R. Z. Khatullin, O. Schütt, F. Schiffmann, D. Golze, J. Wilhelm, S. Chulkov, M. H. Bani-Hashemian, V. Weber, U. Borštnik, M. Taillefumier, A. S. Jakobovits, A. Lazaro, H. Pabst, T. Müller, R. Schade, M. Guidon, S. Andermatt, N. Holmberg, G. K. Schenter, A. Hehn, A. Bussy, F. Belleflamme, G. Tabacchi, A. Glöß, M. Lass, I. Bethune, C. J. Mundy, C. Plessl, M. Watkins, J. VandeVondele, M. Krack, and J. Hutter, Cp2k: An electronic structure and molecular dynamics software package - quickstep: Efficient and accurate electronic structure calculations, *J. Chem. Phys.* **152**, 194103 (2020).
- [63] J. J. Mortensen, L. B. Hansen, and K. W. Jacobsen, Real-space grid implementation of the projector augmented wave method, *Phys. Rev. B* **71**, 035109 (2005).
- [64] J. Enkovaara, C. Rostgaard, J. J. Mortensen, J. Chen, M. Dulak, L. Ferrighi, J. Gavnholt, C. Glinsvad, V. Haikola, H. A. Hansen, H. H. Kristoffersen, M. Kuisma, A. H. Larsen, L. Lehtovaara, M. Ljungberg, O. Lopez-Acevedo, P. G. Moses, J. Ojanen, T. Olsen, V. Petzold, N. A. Romero, J. Stausholm-Møller, M. Strange, G. A. Tritsarlis, M. Vanin, M. Walter, B. Hammer, H. Häkkinen, G. K. H. Madsen, R. M. Nieminen, J. K. Nørskov, M. Puska, T. T. Rantala, J. Schiøtz, K. S. Thygesen, and K. W. Jacobsen, Electronic structure calculations with GPAW: a real-space implementation of the projector augmented-wave method, *J. Phys.: Condens. Matter* **22**, 253202 (2010).
- [65] M. A. Marques, A. Castro, G. F. Bertsch, and A. Rubio, octopus: a first-principles tool for excited electron-ion dynamics, *Comp. Phys. Commun.* **151**, 60 (2003).
- [66] A. Castro, H. Appel, M. Oliveira, C. A. Rozzi, X. Andrade, F. Lorenzen, M. A. L. Marques, E. K. U. Gross, and A. Rubio, octopus: a tool for the application of time-dependent density functional theory, *Phys. Status Solidi (b)* **243**, 2465 (2006).
- [67] X. Andrade, D. Strubbe, U. De Giovannini, A. H. Larsen, M. J. T. Oliveira, J. Alberdi-Rodriguez, A. Varas, I. Theophilou, N. Helbig, M. J. Verstraete, L. Stella, F. Nogueira, A. Aspuru-Guzik, A. Castro, M. A. L. Marques, and A. Rubio, Real-space grids and the octopus code as tools for the development of new simulation approaches for electronic systems, *Phys. Chem. Chem. Phys.* **17**, 31371 (2015).
- [68] A. Hjorth Larsen, M. Kuisma, J. Löfgren, Y. Pouillon, P. Erhart, and P. Hyldgaard, libvdx: A library for exchange-correlation functionals in the vdW-DF family, *Modelling Simul. Mater. Sci. Eng.* **25**, 065004 (2016).
- [69] A. M. de Andrade, J. Kullgren, and P. Broqvist, Quantitative and qualitative performance of density functional theory rationalized by reduced density gradient distributions, *Phys. Rev. B* **102**, 075115 (2020).
- [70] E. Schröder, V. R. Cooper, K. Berland, B. I. Lundqvist, P. Hyldgaard, and T. Thonhauser, The vdW-DF family of non-local exchange-correlation functionals, in *Non-covalent Interactions in Quantum Chemistry and Physics: Theory and Applications*, edited by A. O. de la Roza and G. Di Labio (Elsevier, Amsterdam, 2017).
- [71] J. P. Perdew and Y. Wang, Pair-distribution function and its coupling-constant average for the spin-polarized electron gas, *Phys. Rev. B* **46**, 12947 (1992).
- [72] R. Sabatini, E. Küçükbenli, B. Kolb, T. Thonhauser, and S. de Gironcoli, Structural evolution of amino acid crystals under stress from a non-empirical density functional, *J. Phys.: Condens. Matter* **24**, 424209 (2012).
- [73] O. H. Nielsen and R. M. Martin, Quantum-mechanical theory of stress and force, *Phys. Rev. B* **32**, 3780 (1985).
- [74] T. Y. Tien and L. E. Cross, Dielectric Relaxation in Strontium Titanate Solid Solutions Containing Lanthania, *Jpn. J. Appl. Phys.* **6**, 459 (1967).
- [75] H. Thomas and K. A. Müller, Structural Phase Transitions in Perovskite-Type Crystals, *Phys. Rev. Lett.* **21**, 1256 (1968).
- [76] W. Van Gool and A. G. Piken, Lattice self-potentials and madelung constants for some compounds, *J. Mater.*

- Sci. **4**, 95 (1969).
- [77] M. A. Saifi and L. E. Cross, Dielectric Properties of Strontium Titanate at Low Temperature, Phys. Rev. B **2**, 677 (1970).
- [78] E. Salje, Phase transitions in ferroelastic and co-elastic crystals, Ferroelectrics **104**, 111 (1990).
- [79] T. Nakamura, Soft phonon in BaTiO₃, Ferroelectrics **137**, 65 (1992).
- [80] W. Zhong, D. Vanderbilt, and K. M. Rabe, Phase Transitions in BaTiO₃ from First Principles, Phys. Rev. Lett. **73**, 1861 (1994).
- [81] W. Zhong and D. Vanderbilt, Competing structural instabilities in cubic perovskites, Phys. Rev. Lett. **74**, 2587 (1995).
- [82] W. Zhong, D. Vanderbilt, and K. M. Rabe, First-principles theory of ferroelectric phase transitions for perovskites: The case of BaTiO₃, Phys. Rev. B **52**, 6301 (1995).
- [83] W. Zhong and D. Vanderbilt, Effect of quantum fluctuations on structural phase transitions in SrTiO₃ and BaTiO₃, Phys. Rev. B **53**, 5047 (1996).
- [84] T. Varnhorst, O. F. Schirmer, H. Kröse, R. Scharfschwerdt, and T. W. Kool, O- holes associated with alkali acceptors in BaTiO₃, Phys. Rev. B **53**, 116 (1996).
- [85] D. Vanderbilt and W. Zhong, First-principles theory of structural phase transitions for perovskites: Competing instabilities, Ferroelectrics **206**, 181 (1998).
- [86] B. Meyer and D. Vanderbilt, Ab initio study of BaTiO₃ and PbTiO₃ surfaces in external electric fields, Phys. Rev. B **63**, 205426 (2001).
- [87] R. Resta, Macroscopic Electric Polarization as a Geometric Quantum Phase, Europhys. Lett. **22**, 133 (1993).
- [88] X. Wu, D. Vanderbilt, and D. R. Hamann, Systematic treatment of displacements, strains, and electric fields in density-functional perturbation theory, Phys. Rev. B **72**, 035105 (2005).
- [89] E. K. H. Salje, M. Guennou, P. Bouvier, M. A. Carpenter, and J. Kreisel, High pressure ferroelastic phase transition in SrTiO₃, J. Phys. Condens. Matter **23**, 275901 (2011).
- [90] T. Tadano and S. Tsuneyuki, Self-consistent phonon calculations of lattice dynamical properties in cubic srtio₃ with first-principle anharmonic force constants, Phys. Rev. B **92**, 054301 (2015).
- [91] T. Tadano and S. Tsuneyuki, Ab initio prediction of structural phase-transition temperature of srtio₃ from finite-temperature phonon calculation, J. Ceram. Soc. Jpn. **127**, 404 (2019).
- [92] J. B. Lando, H. G. Olf, and A. Peterlin, Nuclear magnetic resonance and X-ray determination of the structure of poly(vinylidene fluoride), J. Polym. Sci. A Polym. Chem. **4**, 941 (1966).
- [93] R. Hasegawa, Y. Takahashi, Y. Chatani, and H. Tadokoro, Crystal structures of three crystalline forms of poly(vinylidene fluoride), Polym. J. **3**, 600 (1972).
- [94] R. Resta, Manifestations of Berry's phase in molecules and condensed matter, J. Phys. Condens. Matter **12**, R107 (2000).
- [95] K. Nakamura, M. Nagai, T. Kanamoto, Y. Takahashi, and T. Furukawa, Development of oriented structure and properties on drawing of poly(vinylidene fluoride) by solid-state coextrusion, J. Polym. Sci. B Polym. Phys. **39**, 1371 (2001).
- [96] V. Ranjan, L. Yu, M. B. Nardelli, and J. Bernholc, Phase Equilibria in High Energy Density PVDF-Based Polymers, Phys. Rev. Lett. **99**, 047801 (2007).
- [97] V. Ranjan, M. B. Nardelli, and J. Bernholc, Electric Field Induced Phase Transitions in Polymers: a Novel Mechanism for High Speed Energy Storage, Phys. Rev. Lett. **108**, 087802 (2012).
- [98] A. Itoh, Y. Takahashi, T. Furukawa, and H. Yajima, Solid-state calculations of poly(vinylidene fluoride) using the hybrid DFT method: spontaneous polarization of polymorphs, Polym. J. **46**, 207 (2014).
- [99] Y. Zhao, W. Yang, Y. Zhou, Y. Chen, X. Cao, Y. Yang, J. Xu, and Y. Jiang, Effect of crystalline phase on the dielectric and energy storage properties of poly(vinylidene fluoride), J. Mater. Sci. Mater. Electron. **27**, 7280 (2016).
- [100] R. Dong, V. Ranjan, M. B. Nardelli, and J. Bernholc, First-principles simulations of PVDF copolymers with high dielectric energy density: PVDF-HPF and PVDF-BTTFE, Phys. Rev. B **94**, 014210 (2016).
- [101] F. Pelizza, B. R. Smith, and K. Johnston, A van der Waals density functional theory study of poly(vinylidene difluoride) crystalline phases, Eur. Phys. J. Special Topics **225**, 1733 (2016).
- [102] P. A. T. Olsson, E. Schröder, P. Hyldgaard, M. Kroon, E. Andreasson, and E. Bergvall, Ab initio and classical atomistic modelling of structure and defects in crystalline orthorhombic polyethylene: Twin boundaries, slip interfaces, and nature of barriers, Polymer **121**, 234 (2017).
- [103] P. A. T. Olsson, P. Hyldgaard, E. Schröder, E. P. Jutemar, E. Andreasson, and M. Kroon, Ab initio investigation of martensitic transformation in crystalline polyethylene, Phys. Rev. M **2**, 075602 (2018).
- [104] L. Ruan, X. Yao, Y. Chang, L. Zhou, G. Qin, and X. Zhang, Properties and Applications of the β Phase Poly(vinylidene fluoride), Polymers **10**, 228 (2018).
- [105] F. Pelizza and K. Johnston, A density functional theory study of poly(vinylidene difluoride) crystalline phases, Polymer **179**, 121585 (2019).
- [106] D. Vanderbilt and R. D. King-Smith, Electric polarization as a bulk quantity and its relation to surface charge, Phys. Rev. B **48**, 4442 (1993).
- [107] A. Togo, F. Oba, and I. Tanaka, First-principles calculations of the ferroelastic transition between rutile-type and CaCl₂-type SiO₂ at high pressures, Phys. Rev. B **78**, 134106 (2008).
- [108] A. Togo, L. Chaput, I. Tanaka, and G. Hug, First-principles phonon calculations of thermal expansion in Ti₃SiC₂, Ti₃AlC₂, and Ti₃GeC₂, Phys. Rev. B **81**, 174301 (2010).
- [109] I. Tanaka, A. Togo, A. Seko, F. Oba, Y. Koyama, and A. Kuwabara, Thermodynamics and structures of oxide crystals by a systematic set of first principles calculations, J. Mater. Chem. **20**, 10335 (2010).
- [110] Y. Pie and X. C. Zeng, Elastic properties of poly(vinylidene fluoride) (PVDF) crystals: A density functional theory study, J. Appl. Phys. **109**, 093514 (2011).
- [111] A. Togo and I. Tanaka, First principles phonon calculations in materials science, Scr. Mater. **108**, 1 (2015).
- [112] J. M. Skelton, L. A. Burton, S. C. Parker, A. Walsh, C.-E. Kim, A. Soon, J. Buckeridge, A. A. Sokol, C. R. A. Catlow, A. Togo, and I. Tanaka, Anharmonicity in the High-Temperature *Cmcm* Phase of SnSe: Soft Modes

- and Three-Phonon Interactions, *Phys. Rev. Lett.* **117**, 075502 (2016).
- [113] J. M. Skelton, L. A. Burton, A. J. Jackson, F. Oba, S. C. Parker, and A. Walsh, Lattice dynamics of the tin sulphides SnS_2 , SnS and Sn_2S_3 : vibrational spectra and thermal transport, *Phys. Chem. Chem. Phys.* **19**, 12452 (2017).
- [114] F. Eriksson, E. Fransson, and P. Erhart, The hiphive package for the extraction of high-order force constants by machine learning, *Adv. Theory Simul.* **2**, 1800184 (2019).
- [115] E. Fransson, F. Eriksson, and P. Erhart, Efficient construction and applications of higher-order force constant models, *Npj. Comput. Mater.* **6**, 135 (2020).
- [116] W. Setyawan and S. Curtarolo, High-throughput electronic band structure calculations: Challenges and tools, *Comput. Mater. Sci.* **49**, 299 (2010).
- [117] J. Repp, G. Meyer, K.-H. Rieder, and P. Hyldgaard, Site determination and thermally assisted tunneling in homogeneous nucleation, *Phys. Rev. Lett.* **91**, 206102 (2003).
- [118] S. J. Stranick, M. M. Kamna, and P. S. Weiss, Atomic-Scale Dynamics of a Two-Dimensional Gas-Solid Interface, *Science* **266**, 99 (1994).
- [119] S. J. Stranick, M. M. Kamna, and P. S. Weiss, Interactions and dynamics of benzene on $\text{Cu}\{111\}$ at low temperature, *Surf. Sci.* **338**, 41 (1995).
- [120] A. Bogicevic, P. Hyldgaard, G. Wahnström, and B. I. Lundqvist, Al Dimer Dynamics on $\text{Al}(111)$, *Phys. Rev. Lett.* **81**, 172 (1998).
- [121] P. Hyldgaard and M. Persson, Long-ranged adsorbate-adsorbate interactions mediated by a surface-state band, *J. Phys.:Condens. Matter* **12**, L13 (2000).
- [122] J. Repp, F. Moresco, G. Meyer, K.-H. Rieder, P. Hyldgaard, and M. Persson, Substrate Mediated Long-Range Oscillatory Interaction between Adatoms: $\text{Cu}/\text{Cu}(111)$, *Phys. Rev. Lett.* **85**, 2981 (2000).
- [123] K. Berland, T. L. Einstein, and P. Hyldgaard, Rings sliding on a honeycomb network: Adsorption contours, interactions, and assembly of benzene on $\text{Cu}(111)$, *Phys. Rev. B* **80**, 155431 (2009).
- [124] P. Han and P. S. Weiss, Electronic substrate-mediated interactions, *Surf. Sci. Rep.* **67**, 19 (2012).
- [125] R. D. King-Smith and D. Vanderbilt, Theory of polarization of crystalline solids, *Phys. Rev. B* **47**, 1651 (1993).
- [126] S. Baroni and R. Resta, Ab initio calculation of the macroscopic dielectric constant in silicon, *Phys. Rev. B* **33**, 7017 (1986).
- [127] R. W. Nunes and X. Gonze, Berry-phase treatment of the homogeneous electric field perturbation in insulators, *Phys. Rev. B* **63**, 155107 (2001).
- [128] I. Souza, J. Iniguez, and D. Vanderbilt, First-Principles Approach to Insulators in Finite Electric Fields, *Phys. Rev. Lett.* **89**, 117602 (2002).
- [129] M. Gajdoš, K. Hummer, G. Kresse, J. Furthmüller, and F. Bechstedt, Linear optical properties in the projector-augmented wave methodology, *Phys. Rev. B* **73**, 045112 (2006).
- [130] H. J. Monkhorst and J. D. Pack, Special points for Brillouin-zone integrations, *Phys. Rev. B* **13**, 5188 (1976).
- [131] A. M. Glazer, The classification of tilted octahedra in perovskites, *Acta Crystallogr. Sect. B Struct. Crystallogr. Cryst. Chem.* **28**, 3384 (1972).
- [132] A. M. Glazer, Simple ways of determining perovskite structures, *Acta Crystallogr. Sect. A* **31**, 756 (1975).
- [133] D. R. Hamann, Optimized norm-conserving Vanderbilt pseudopotentials, *Phys. Rev. B* **88**, 085117 (2013).
- [134] M. Schlipf and F. Gygi, Optimization algorithm for the generation of ONCV pseudopotentials, *Comput. Phys. Commun.* **196**, 36 (2015).
- [135] E. Ziambaras and E. Schröder, Theory for structure and bulk modulus determination, *Phys. Rev. B* **68**, 064112 (2003).
- [136] D. P. Harding, L. J. Kingsley, G. Spraggon, and S. E. Wheeler, Importance of model size in quantum mechanical studies of DNA intercalation, *J. Comput. Chem.* **41**, 1175 (2020).
- [137] P. Sanden, K. Börjesson, H. Li, J. Mårtensson, T. Brown, L. M. Wilhelmsson, and B. Albinsson, Characterization and use of an unprecedentedly bright and structurally non-perturbing fluorescent DNA base analogue, *Nucleic Acids Res.* **36**, 157 (2007).
- [138] M. S. Wranne, A. F. Füchtbauer, B. Dumat, M. Bood, A. H. El-Sagheer, T. Brown, H. Graden, M. Grötl, and L. M. Wilhelmsson, Towards Complete Sequence Flexibility of Nucleic Acid Base Analogue FRET, *J. Am. Chem. Soc.* **139**, 9217 (2017).
- [139] S. Andermatt, J. Cha, F. Schiffmann, and J. VandeVondele, Combining linear-scaling dft with subsystem dft in born-oppenheimer and ehrenfest molecular dynamics simulations: From molecules to a virus in solution, *J. Chem. Theo. Comput.* **12**, 3214 (2016).
- [140] J. Kleis and E. Schröder, van der Waals interaction of simple, parallel polymers, *J. Chem. Phys.* **122**, 164902 (2005).
- [141] J. Kleis, P. Hyldgaard, and E. Schröder, van der Waals interaction of parallel polymers and nanotubes, *Comp. Mater. Sci.* **33**, 192 (2005).
- [142] J. Kleis, B. I. Lundqvist, D. C. Langreth, and E. Schröder, Towards a working density-functional theory for polymers: First-principles determination of the polyethylene crystal structure, *Phys. Rev. B* **76**, 100201 (2007).
- [143] J. Kleis, E. Schröder, and P. Hyldgaard, Nature and strength of bonding in a crystal of semiconducting nanotubes: van der Waals density functional calculations and analytical results, *Phys. Rev. B* **77**, 205422 (2008).
- [144] G. Makov and M. C. Payne, Periodic boundary conditions in ab initio calculations, *Phys. Rev. B* **51**, 4014 (1995).
- [145] L. Goerigk, A. Hansen, C. Bayer, S. Ehrlich, A. Najibi, and S. Grimme, A look at the density functional theory zoo with the advanced gmtkn55 database for general main group thermochemistry, kinetics and noncovalent interactions, *Phys. Chem. Chem. Phys.* **19**, 32184 (2017).
- [146] T. Rangel, K. Berland, S. Sharifzadeh, F. Brown-Altwater, K. Lee, P. Hyldgaard, L. Kronik, and J. B. Neaton, Structural and excited-state properties of oligoacene crystals from first principles, *Phys. Rev. B* **93**, 115206 (2016).
- [147] D. Lee, F. Furche, and K. Burke, Accuracy of electron affinities of atoms in approximate density functional theory, *J. Phys. Chem. Lett.* **1**, 2124 (2010).
- [148] A. Perrichon, E. J. Granhed, G. Romanelli, A. Piovano, A. Lindman, P. Hyldgaard, G. Wahnström, and

- M. Karlsson, Unraveling the ground-state structure of BaZrO_3 by neutron scattering experiments and first-principle calculations, *Chem. Mater.* **32**, 2824 (2020).
- [149] M. A. Helal, T. Mori, and S. Kojima, Softening of infrared-active mode of perovskite BaZrO_3 proved by terahertz time-domain spectroscopy, *Appl. Phys. Lett.* **106**, 182904 (2015).
- [150] K. Goretta, E. Park, R. Koritala, M. Cuber, E. Pascual, N. Chen, A. de Arellano-López, and J. Routbort, Thermomechanical response of polycrystalline BaZrO_3 , *Physica C Supercond.* **309**, 245 (1998).
- [151] M. Helal and S. Kojima, Structural instability and phase transition in BaZrO_3 single crystals: Brillouin scattering and DFT study, *Mater. Sci. Eng. B Solid* **271**, 115314 (2021).
- [152] A. R. Akbarzadeh, I. Kornev, C. Malibert, L. Bellaiche, and J. M. Kiat, Combined theoretical and experimental study of the low-temperature properties of BaZrO_3 , *Phys. Rev. B* **72**, 205104 (2005).
- [153] M. Schmidbauer, A. Kwasniewski, and J. Schwarzkopf, High-precision absolute lattice parameter determination of SrTiO_3 , DyScO_3 and NdGaO_3 single crystals, *Acta Cryst. B* **68**, 8 (2012).
- [154] R. O. Bell and G. Rupprecht, Elastic Constants of Strontium Titanate, *Phys. Rev.* **129**, 90 (1963).
- [155] R. Wahl, D. Vogtenhuber, and G. Kresse, SrTiO_3 and BaTiO_3 revisited using the projector augmented wave method: Performance of hybrid and semilocal functionals, *Phys. Rev B* **78**, 104116 (2008).
- [156] K. A. Müller and W. Berlinger, Static critical exponents at structural phase transitions, *Phys. Rev. Lett.* **26**, 13 (1971).
- [157] K. Lejaeghere, V. V. Speybroeck, G. V. Oost, and S. Cottener, Error estimates for solid-state density-functional theory predictions: An overview by means of the ground-state elemental crystals, *Crit. Rev. Sol. State Mater. Sci.* **39**, 1 (2014).
- [158] W.-T. Chen, F. Sher, N. D. Mathur, C. M. Kavanagh, F. D. Morrison, and J. P. Attfield, Structural, magnetic, and electrical properties of $\text{Bi}_{1-x}\text{La}_x\text{MnO}_3$ ($x = 0.0, 0.1$, and 0.2) solid solutions, *Chem. Mater.* **24**, 199 (2012).
- [159] H. Jeen, G. Singh-Bhalla, P. R. Mickel, K. Voigt, C. Morien, S. Tongay, A. F. Hebard, and A. Biswas, Growth and characterization of multiferroic BiMnO_3 thin films, *J. Appl. Phys.* **109**, 074104 (2011).
- [160] A. D. Becke and E. R. Johnson, Exchange-hole dipole moment and the dispersion interaction revisited, *J. Chem. Phys.* **127**, 154108 (2007).
- [161] S. Grimme, J. Antony, S. Ehrlich, and H. Krieg, A consistent and accurate ab initio parametrization of density functional dispersion correction (DFT-D) for the 94 elements H–Pu, *J. Chem. Phys.* **132**, 154104 (2010).
- [162] H. M. Berman, J. Westbrook, Z. Feng, G. Gilliland, T. N. Bhat, H. Weissig, I. N. Shindyalov, and P. E. Bourne, The Protein Data Bank, *Nucleic Acids Res.* **28**, 235 (2000).
- [163] A. G. Császár, W. D. Allen, and H. F. Schaefer, In pursuit of the ab initio limit for conformational energy prototypes, *J. Chem. Phys.* **108**, 9751 (1998).
- [164] A. J. Lovinger, Unit cell of the α phase of poly(vinylidene fluoride), *Macromolecules* **14**, 322 (1981).
- [165] R. Resta and D. Vanderbilt, Theory of Polarization: A Modern Approach, in *Phys. Ferroelectr.* (Springer Berlin Heidelberg, Berlin, Heidelberg, 2007) pp. 31–68.